

Temperature dependence of the crystal growth rate of $\text{Ge}_x\text{Sb}_{1-x}$ phase-change alloys using laser irradiated crystallization measurements

Tobias Van Damme (s1738410)
Daily supervisor: dr. ir. G. Eising
Supervisor: Prof. dr. ir. B. Kooi

Zernike Institute for Advanced Materials
University of Groningen

November 3, 2014

Abstract

To obtain a proper understanding of the crystallization nature of $\text{Ge}_x\text{Sb}_{1-x}$ alloys, with compositions $x = 6, 7, 8, 9, 10$, depending on the temperature, the crystal growth rate has to be measured over a large range of temperatures. Previously isothermal measurement as well as measurements with a low intensity laser spot have been performed. By focusing a laser beam a smaller, more intense laser spot of $250 \mu\text{m} \times 110 \mu\text{m}$ was obtained. With this laser spot it was possible to measure in higher temperature regimes than previously possible. It is found that the laser spot only locally heats the sample and thus only locally crystallizes the sample. To determine the temperature at the locally measured area a calibration has been made with the lowest germanium content composition studied here, $\text{Ge}_6\text{Sb}_{94}$. By assuming Arrhenius behavior for $\text{Ge}_6\text{Sb}_{94}$ up to the high temperature regime, it is possible to measure the heat added by the laser. This calibration is then used to determine the local temperature during measurements of the higher germanium content composition. As expected deviation from the Arrhenius behavior is observed. To complete our understanding of the different compositions over the whole temperature range, the viscosity is calculated from the measured growth rates. Using the VFT model and more recently proposed Mauro model it is possible to obtain a relation of the viscosity over the complete temperature range from glass transition temperature, T_g to the melting temperature, T_m . Converting back to the crystal growth rate, maximum possible growth rates up to $\sim 10 \text{ m s}^{-1}$ are found. Also the fragility and the glass transition temperature of the different compositions is calculated. For the fragility values between $m = 46-68$ (Mauro) and $m = 60-109$ (VFT) and for the glass temperatures values of $T_g = 324-430$ (Mauro) and $T_g = 331-443$ (VFT) are found. Following a side track incorporating the use of gold nanoparticles to increase the local temperature during a laser measurement, gold nanoparticles were deposited on the surface of a $\text{Ge}_8\text{Sb}_{92}$ sample. Although no major improvements in crystal growth were found, there are strong indications that the nanoparticles do in fact increase the crystal growth rate.

Contents

1	Introduction	3
2	Theory	6
2.1	Nucleation and growth	6
2.2	Viscosity models and fragility	7
3	Experimental	9
3.1	Samples	9
3.2	Measurement setup	9
3.3	Image analysis	10
3.4	Laser profile	12
3.5	Analysis of laser induced growth rate profile	14
4	Results and discussions	16
4.1	Crystal growth rate in the high temperature domain	16
4.2	Influence of experimental parameters on added laser heat	18
4.3	Viscosity model	19
5	Other work	25
5.1	Gold nanorods and surface plasmons	25
6	Conclusions	30
7	Recommendations	31
8	References	32

I Introduction

The invention of the computer sparked the beginning of a new era of technological advancements. Where the first computer was as large as 100 m², nowadays it is possible to have a computer the size of small lunch box. Not only has the size decreased but the computing power has increased enormously. One area of interest when concerning computers is data storage, both for long-term storage as well as short-term storage. With the introduction of the compact disk (CD) and CD-rewritable, phase-change materials (PCM) were first introduced in real life applications. After being pushed to the background, PCM's are now becoming more and more popular for use within memory and data storage applications.

Phase-change materials are materials which are able to switch between different phases which generally are based on a highly ordered crystalline state and a disordered amorphous state. The crystalline phase is characterized by low electrical resistance and high reflectivity whereas the amorphous phase has a high electrical resistance and a low reflectivity. Since computer data consists of ones and zeros, one can use the two phases of a PCM to depict the '0' (amorphous) and '1' (crystalline).

As early as 1968, research [1] has been done on these type of materials. Unfortunately due to low crystallization speeds and high energy consumption, the research on these materials was pushed to the background. Only after the introduction of the Compact Disk-Read Only Memory (CD-ROM) phase-change materials came back in the picture. Research was done in the late 80s [2,3] on the possibilities to use a GeTe alloy in rewritable optical disks. It took until 1997 before these disks were commercially introduced. After this, further optimization of material properties led to increased data storage capabilities, from 650 MB in compact disks to 4.7 GB in digital versatile disk (DVD) to 23.3 GB (single-layer) or 50 GB (dual-layer) blu-ray disks (BD).

Besides GeTe, also Ge₁₁Te₆₀Sn₄Au₂₅ was a promising material [4,5] with fast recrystallization and good optical contrast. Because of these developments new alloys were found, such as Ge₁Sb₄Te₇, Ge₁Sb₂Te₄ and Ge₂Sb₂Te₅ [3,6], continuing with doped Sb₂Te, with dopants such as Ag, In and Ge [7–9]. A good example is Ag₅In₅Sb₆₀Te₃₀ (AIST), this alloy has many uses in rewritable DVD's [10]. A third type of material that has been found later on is Ge-doped Sb [11]. Because of the constant developments in crystallization speed and material properties of PCM's, they are not only interesting as external optical data storage but have also become competitive with current day dynamic random access memory (DRAM) [12–17].

In Figure 1 a schematic is given of the workings of a single PCM data cell. Via laser pulses the phase of the cell can be switched between amorphous and crystalline. In the example the cell starts in the amorphous state. An applied pulse will heat the material to the temperature regime, below melting temperature, where the PCM will rapidly crystallize. After sufficient time the cell is crystallized and the pulse is switched off. The state of the cell can now be read out with a low power laser beam which has high enough power to do an accurate read out but has low enough power such that the state of the cell is not altered. To amorphize the cell again a 'reset' pulse is used. The pulse heats the cell to above the melting temperature, melting the PCM. By super fast cooling the disordered liquid state can be 'frozen' creating the amorphous state of the PCM. Again a read pulse is such that it will not alter the state of the PCM. As mentioned before the read out of the PCM cell can be done via two ways, one can measure the reflectivity of the cell or measure the conductivity of the cell. Similarly, instead of laser pulses one can also use electrical pulses to switch between the two phases and therefore it is possible to make a completely electronic based RAM (random access memory) type memory.

The performance of PCM's is among other aspects based on the time necessary to switch between the

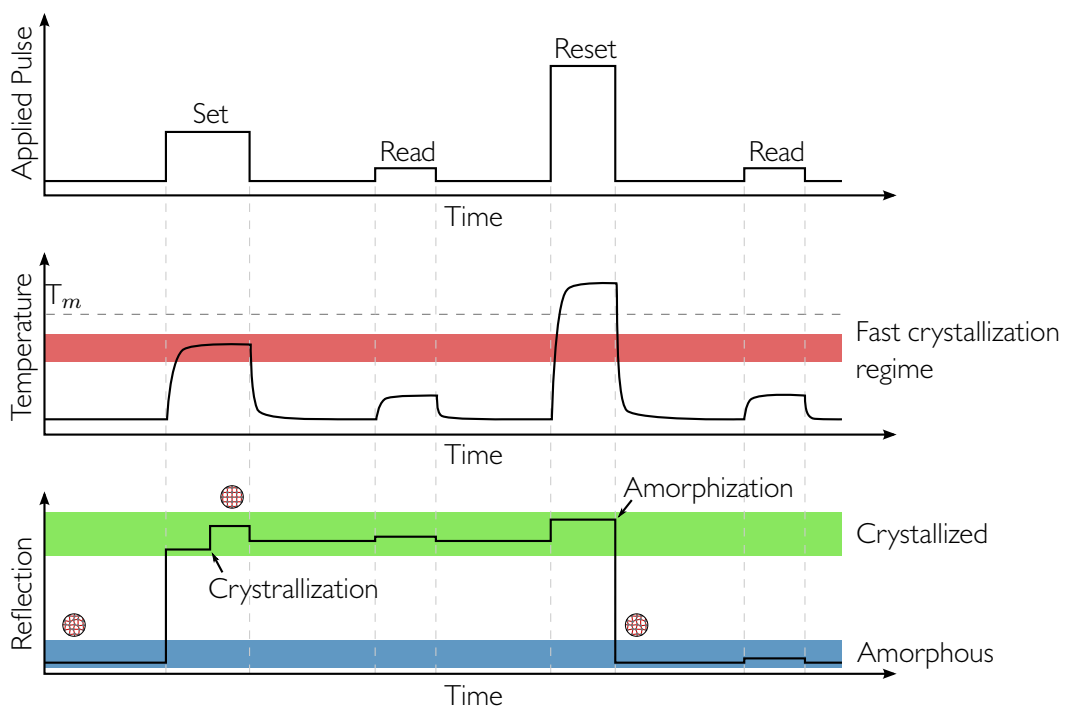


Figure 1: Schematic of writing and erasing a PCM data cell. The cell starts in the amorphous state, then an applied pulse such that the cell heats enough to enter the fast crystallization regime will crystallize the cell. A weak signal can then be used to read out the cell. The added heat of the beam will not be enough to alter the phase. A reset pulse will heat to the cell to above the melting temperature. During cooling the cell cools very rapidly making sure the cell has no time to recrystallize, 'freezing' the cell back in the amorphous state. An additional read pulse can again read out the state without altering the phase of the cell.

crystallized and amorphous state and the ability to retain data, in case of long-term storage options. During writing and erasing the respective crystallization and amorphizing should be done as fast as possible, while at normal operating conditions the material should not crystallize or amorphize at all. Since the performance is determined by the temperature dependent behavior of these materials, it is very interesting and relevant to study the temperature response of phase-change materials. The materials of interest in this research are $\text{Ge}_x\text{Sb}_{1-x}$ -alloys. This is a new class of materials which has not been greatly studied in the past. Antimony is a very fast crystallization agent while Germanium is used to stabilize the alloy and allow amorphizing of the material. Because of the pronounced optical contrast between the crystalline and amorphous phase it is possible to study the crystallization optically.

Aim of this research Up to now only isothermal measurements have been done. This involves heating complete samples and measuring details of the crystallization process (e.g. incubation, nucleation and growth). With this technique it is only possible to measure the crystal growth rate in a limited temperature range. To extend the measurement range we use a laser to locally heat the sample to higher temperature than what was previously possible. This is also in line with reality where a laser is used as a cell 'set' and 'reset' pulse. With a high-speed optical camera it is possible to record the measurement and determine the crystal growth rate. By varying the laser power we can vary the local temperature increase. Since the crystal growth rate is only temperature dependent we expect to measure different crystallization rates. The main focus of this thesis will be to find a relation between the crystallization speed and the temperature of $\text{Ge}_x\text{Sb}_{1-x}$ with compositions $x = 6, 7, 8, 9$ and 10 . To determine the temperature-dependent behavior we first will investigate the relation between the temperature increase induced by a certain amount of laser power.

For the isothermal measurements it has been observed that the crystal growth rate is dependent on temperature according to standard Arrhenius behavior. For higher temperatures it is expected that deviation from the Arrhenius behavior occurs, as is seen for example in $\text{Ge}_2\text{Sb}_2\text{Te}_5$ [18]. Combining the isothermal measurements with the results from the laser measurements we will attempt to extrapolate the temperature dependent behavior from very low temperatures up to the melting temperature. To that end we will use the connection between the crystal growth rate and the viscosity of a given material. While it is not known what the temperature dependent crystal growth rate for GeSb-alloys looks like for the full temperature range, there are popular models to fit the viscosity in this range. Using this approach we can then also calculate the so-called fragility of the undercooled liquids of the compositions.

In this report first the relevant theory will be reviewed, Section 2. In Section 3, the experimental setup will be reviewed and a detailed description will be given of the software used to analyze the measurements. Also an example of the analysis of a measurement will be given. The results will be discussed in Section 4, where the calibration for the added heat of the laser beam and the extrapolation to the full temperature range will be discussed. An interesting side track is discussed in Section 5. Here it is investigated whether the localized surface plasmon resonance of gold nanoparticles can contribute to an increased crystal growth rate. The report ends with conclusions in Section 6, and recommendations for further research, Section 7.

2 Theory

2.1 Nucleation and growth

Based on the work of the Dutch chemist Van 't Hoff, Arrhenius proposed that a formula existed for the rates of both forward and reverse reactions. In his work Arrhenius also provided a physical justification and interpretation of the formula [19,20]. Although the equation is best seen as an empirical relationship, the equation is still remarkably accurate. The Arrhenius equation is given by

$$k = A \exp\left(-\frac{E_a}{k_b T}\right), \quad (1)$$

where k is the rate constant, T the temperature in K, E_a the activation energy in eV, k_b the Boltzmann constant and A is a prefactor.

For the case of crystal growth, distinction is made between growth of the crystal and nucleation of the crystal. A crystal first has to nucleate before it can grow. The kinetics of transformations that occur through nucleation and growth of particles under isothermal annealing conditions are described by isothermal Johnson-Mehl-Avrami-Kolmogorov (JMAK) equation: [21–28]

$$x(t) = 1 - \exp(-kt^n), \quad (2)$$

$$k(T) = k_0 \exp\left(-\frac{\Delta H}{k_b T}\right). \quad (3)$$

These equations describe the volume fraction of the transformed material, x , as function of the time, t , and annealing temperature, T , in terms of the isothermal JMAK parameters, n , ΔH and k_0 . The JMAK parameters can be expressed in terms of the individual nucleation and growth parameters. [29–33] The Avrami exponent, n , can be written as:

$$n = a + bc, \quad (4)$$

where a is the nucleation index, which governs the time dependence of the number of nuclei per unit volume of untransformed material, N , as a function of time: [34]

$$N \propto t^n, \quad (5)$$

b is the dimensionality of growth ($b = 1, 2, 3$ for respectively one-, two- or three-dimensional growth, i.e. where crystals respectively grow in spikes, circles or spheres) and c is the growth index ($c = 1$ for interface-controlled growth and $c = 0.5$ for diffusion-controlled growth).

From the time dependence of the number of nuclei given in Equation 5, the nucleation rate per unit volume of untransformed material, I , changes with t^{a-1} . Assuming an Arrhenius temperature dependence for the nucleation rate [32], we have

$$I(T) = I_0 t^{a-1} \exp\left(-\frac{E_n}{k_b T}\right), \quad (6)$$

where E_n is the activation energy for nucleation and I_0 is a time and temperature independent constant. The time-independent growth rate of the crystals, G , also an Arrhenius temperature dependence can be formulated: [32]

$$G(T) = G_0 \exp\left(-\frac{E_g}{k_b T}\right), \quad (7)$$

where E_g is the activation energy for growth and G_0 is a time and temperature independent constant. Given Equation 6 and Equation 7 it can be shown [35] that the effective activation energy can be given as

$$\Delta H = E_n + bcE_g. \quad (8)$$

As established by Ranganathan and von Heimendahl [32] it can be shown [35] that the relationship between the pre-exponential constants, k_0 , I_0 and G_0 , can be approximated as

$$\ln k_0 = \ln I_0 + bc \ln G_0. \quad (9)$$

For this research it is seen that crystallization is mainly dominated by interface-controlled crystal growth, as will be explained in Section 3. For interface-controlled growth the growth is dominated by atoms jumping from the amorphous configuration to the growing crystal structure. As an atom jumps it conforms to the crystal structure as that is the energy minimal configuration, resulting in a growing crystal. This is a temperature dominated process as is also seen from Equation 7 and is explained in more detail in ref [36]. Intuitively this is easily understood as increased temperature indicates higher atom movement and thus it is easier for the atom to jump from one grain to the other.

2.2 Viscosity models and fragility

To determine the maximum growth rate of different materials it is necessary to extrapolate from the highest measured temperature up to the melting temperature. Since it is not possible to directly extrapolate the crystal growth, as it is unknown how the growth rate behaves depending on temperature, a different method is required. Work has been done on the modeling the dependency of the viscosity on the temperature. While it is still not fully understood what the complete mechanics behind this dependency is, some empirical models were successfully devised which are able to approximate the behavior quite accurately. The most popular model is the Vogel-Fulcher-Tammann(VFT) model [37]. This model however shows systematic errors when extrapolating to low temperatures, thus recent work done by Mauro et al. [38] focused on improving these shortcomings. As the viscosity and the crystal growth are related, these models are used to extrapolate the crystal growth rate to higher temperatures.

The model as proposed by VFT is given as:

$$\log_{10} \eta(T) = \log_{10} \eta_{\infty} + \frac{(12 - \log_{10} \eta_{\infty})^2}{m(T/T_g - 1) + (12 - \log_{10} \eta_{\infty})}, \quad (10)$$

and the model defined by Mauro is given as:

$$\log_{10} \eta(T) = \log_{10} \eta_{\infty} + (12 - \log_{10} \eta_{\infty}) \frac{T_g}{T} \exp \left[\left(\frac{m}{12 - \log_{10} \eta_{\infty}} - 1 \right) \left(\frac{T_g}{T} - 1 \right) \right], \quad (11)$$

where η_{∞} is the viscosity at infinite temperature, m is the fragility and T_g is the glass temperature.

To calculate the viscosity from the crystal growth rate the following equation is used [39, 40]:

$$\eta(T) = \frac{4r_{\text{atom}}k_bT}{3\pi\lambda^2R_{\text{hyd}}u(T)} \left(1 - \exp \left(-\frac{\Delta G(T)}{k_bT} \right) \right), \quad (12)$$

where r_{atom} is the atomic radius, λ the diffusional jump distance, R_{hyd} the hydrodynamic radius, k_b the Boltzmann constant, $u(T)$ the crystal growth rate and $\Delta G(T)$ the Gibbs free energy. The Thomson-Saepen approximation is used to estimate the gain in Gibbs free energy [41]:

$$\Delta G(T) = \Delta H_m \frac{T_m - T}{T_m} \left(\frac{2T}{T_m + T} \right), \quad (13)$$

with ΔH_m the heat of fusion and T_m the melting temperature.

With these models both the glass temperature and the fragility of the modeled material can be determined. The fragility in this sense has no relation with the common usage of the word to mean brittleness. Instead it can be seen as a measure of the deviation from the Arrhenius behavior. Fragile liquids are those that have a high fragility, whereas 'strong' liquids have low fragility and behave according to, or close to, the Arrhenius behavior; i.e. $\eta \propto \frac{1}{T}$. For the Mauro model, a fragility of 15 corresponds to perfect Arrhenius behavior and denotes the order of magnitude difference between the viscosity defined for the glass temperature (10^{12} Pa s) and the melting temperature (10^{-3} Pa s).

3 Experimental

3.1 Samples

The samples used for the experiments in this research are phase-change films deposited on glass substrates. The samples consist of a 200 nm $\text{Ge}_x\text{Sb}_{100-x}$ phase-change film on a 1.3 mm thick glass substrate. To prevent the samples from oxidizing, a finishing layer of 5nm of ZnS-SiO_2 was deposited on top of the phase-change film without breaking the vacuum. The samples were deposited with a Unaxis Sputter coater at a deposition rate of 2.5 nms^{-1} . The composition of the phase-change layer varied between $x = 6, 7, 8, 9, 10$. The composition was chosen by varying the power with which the targets were operated during the deposition process.

The samples were originally sputtered on a $30 \text{ mm} \times 30 \text{ mm}$ surface. This was later cut in smaller squares of $5 \text{ mm} \times 5 \text{ mm}$ by first coating the samples with a μm -layer of PMMA and then cutting with a diamond-tipped glass cutter. The PMMA was removed by first applying acetone and then isopropyl alcohol. The isopropyl was removed from the surface by blow-drying using nitrogen.

The samples were provided by Gert Eising [42] in their final form. So no sample processing was done in the course of this research.

3.2 Measurement setup

The crystallization of the phase-change films was observed using a Photron Fastcam 1024 PCI high-speed optical camera with a Navitar Zoom 6000 objective, capable of recording up to 100 000 frames per second (fps). At the maximum recording rate only a limited resolution is available. Therefore a recording rate of 1000 fps was chosen with a corresponding resolution of 1024 pixels \times 1024 pixels. The objective was extended with a 3mm fine focus and a light source input for coaxial illumination. The latter allows for direct lightening of the sample. Direct lightening is crucial for observing crystals in an amorphous film, as it greatly enhances the contrast due to the specular reflection of the observed films.

Samples were placed on a Watlow Ultramic 600 ceramic heater, capable of heating the sample up to 400°C with a maximum ramp rate of 100°C s^{-1} . The hot plate is mounted in an aluminum holder which is placed on insulating Teflon legs on a stack of three Standa 8MTI 67-25LS motorized translation stages for X-Y movement.

For writing crystalline marks in the amorphous films, and to locally induce additional heating in the phase-change films, a 640 nm diode laser (OBIS 640LX) with variable output power (40 mW - 100 mW) is used. The onset time for the laser to reach this power is less than 2 ns. Different optics are installed allowing the laser to be focused to a sub-micrometer spot for writing and erasing marks, as well as heating the film, in an elliptical area with radii of $a \approx 250\mu\text{m}$ and $b \approx 110\mu\text{m}$. The laser beam is positioned at an incident angle equal to the Brewster's angle, $\theta_B \approx 13^\circ$ for the used films [43]. Characteristic for the Brewster's angle is that the reflection of the laser light on the film is minimized and the coupling of the laser with the material is maximized. The duration of the used pulses is 1.4 s. This duration was long enough to obtain a constant growth rate around the center of the spot.

The whole setup is computer controlled by custom software written by Gert Eising. The software allows for simultaneous recording of the crystal growth and applying of the laser pulse to the film. A PID controller is used to control the power supply of the hot plate. This controller keeps the temperature of

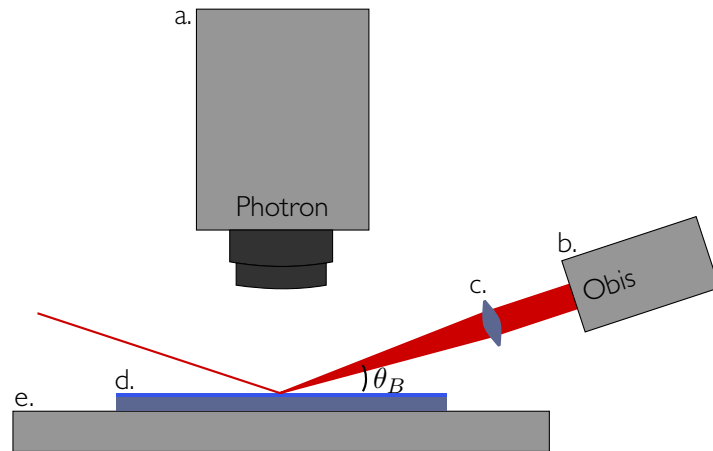


Figure 2: Schematic of laser setup. a) Photron high speed camera. b) Obis 640 nm laser. c) Focusing lens d) Sample consisting of a 200 nm GeSb film on a 1.3 mm thick glass substrate. e) Ceramic heating plate. The incident angle of the laser beam should be close to the Brewster's angles to ensure maximal coupling with the sample and minimal reflection.

the hot plate stable within $\pm 0.1^\circ\text{C}$ of the set temperature. The software also allows for temperature programs.

3.3 Image analysis

The images recorded by the high speed camera are analyzed offline with the help of Matlab software. Due to the great contrast between the amorphous and crystalline phase, the crystal growth can be followed in great detail. The crystal growth rate was obtained by analyzing 100-300 images taken from the high speed recordings, based on a procedure developed by Oosthoek [44] and improved by Eising [42]. In Figure 3 the analysis process is depicted. In Figure 3a an example image is shown. The crystalline (light gray) areas are clearly visible among the amorphous (dark gray) areas due to the high contrast difference between the two phases. From this image a background is subtracted such that only the newly grown crystals remain, Figure 3b. An image taken right before the measurement started acts as the background. Using thresholding techniques the crystals are identified and a binary image is generated with a '1' for crystalline areas and a '0' for amorphous areas, Figure 3c. Due to dust on the surface or irregularities in the layer, noise and speckles appear in the image. With binary open and close operation these disturbances are removed, Figure 3d. Finally with Sobel edge detection the crystalline-amorphous interfaces are found and the pixels at the interface are given the time-value at which the edge appeared at that location, Figure 3e. After repeating steps a to e for every image, a time map can be composed, Figure 3f. Note that in this image the number of data points is greatly reduced for displaying purposes only. The time between each successive line is 160 s and each interface has been thickened to more than one pixel.

The growth rate of the crystals is evaluated along a line. In Figure 3g the line profile is taken along the indicated blue line. The value of each pixel (time at which this position was reached) along the line is plotted versus the position, Figure 3h. From the reciprocal of the slope the growth rate is then calculated. The final growth rate is obtained from averaging the growth rate in various regions of the image.

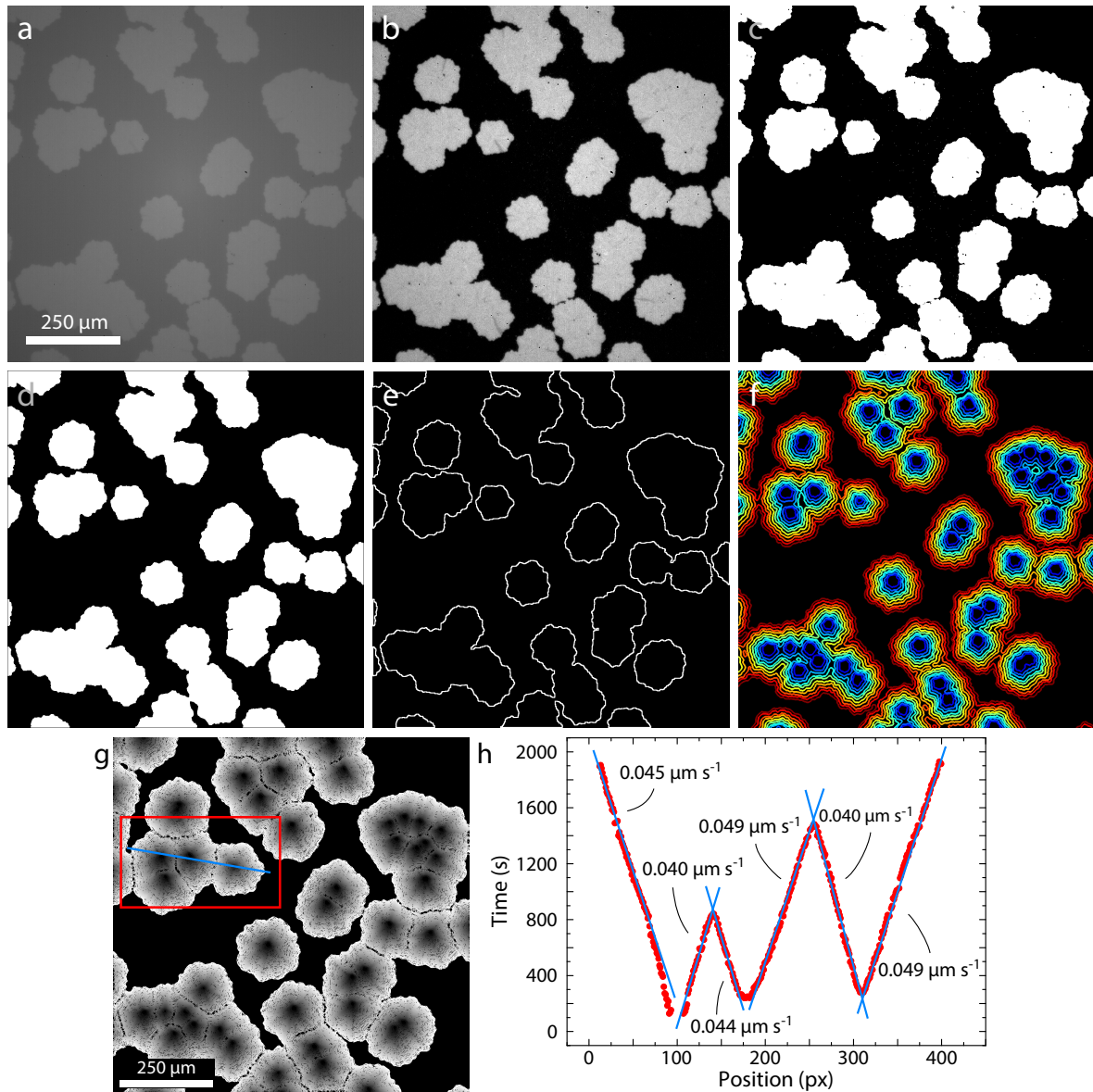


Figure 3: Process of image analysis of crystal growth measurements. **a)** Example image during isothermal measurement as obtained by the optical camera. A clear contrast difference between the amorphous (dark gray) area and the crystalline (light gray) area is seen. **b)** The amorphous background is subtracted from the image by subtracting an image taken before the measurement started. **c)** Using thresholds a binary image is creating with a '0' for amorphous regions and a '1' for crystalline regions. **d)** Binary open and close operations are used to clear the crystal from noise and speckles. **e)** Using Sobel edge detection, the crystalline-amorphous interfaces are determined. Each pixel of the interface receives a value corresponding with the time at which the interface arrived at that pixel. **f)** Repeating steps a to e for every image in the analysis and combining all results in one image, yields a time map of the crystal growth. For displaying purposes the number of lines is greatly reduced with 160 s between each growth front. The lines are also thickened to more than one pixel. **g)** Complete analysis of measurement. The crystal growth rate is analyzed along a line. The blue line indicates the line along which the line profile was taken. **h)** The time at which the interface crossed that position is plotted versus the position. From the reciprocal of the slope, the growth rate is found. For isothermal measurements a line profile is done at several positions and an average for the growth rate is taken. Figure is adapted from ref [42] with permission of Gert Eising.

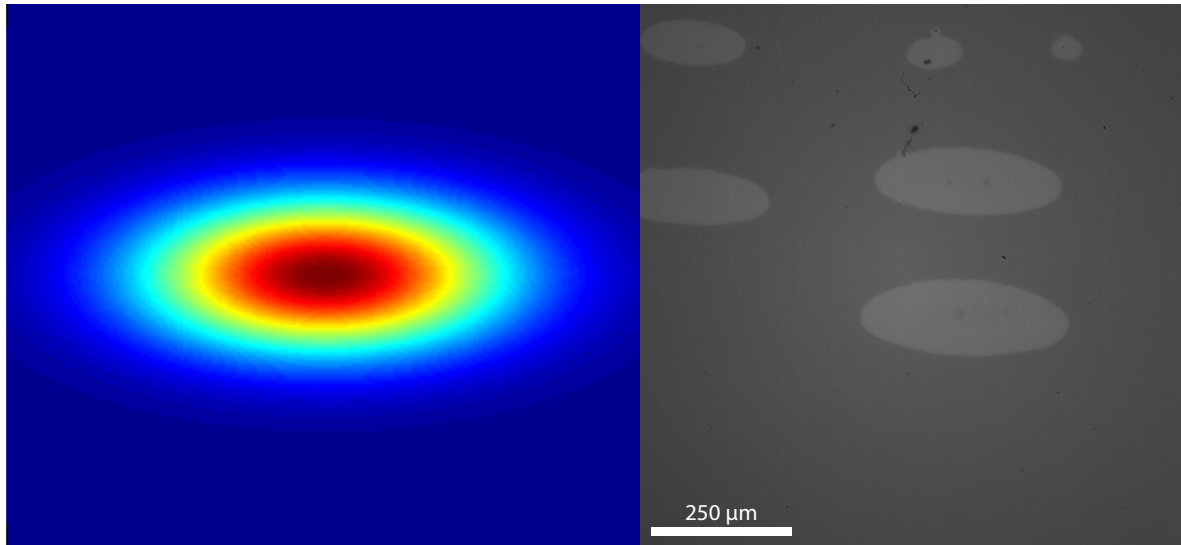


Figure 4: Left: Schematic of laser profile as it hits the surface of the sample. The shape of the laser beam is circular. However as the laser irradiates the sample at an angle, the laser profile is elliptical as it hits the surface. The colors indicate the intensity of the laser going from the maximum temperature in the center to the minimum temperature at the edges. Right: Example of local crystal growth induced by the laser. Because of the profile of the laser, the crystals also have the shape of an ellipse. Crystalline regions only grow locally where the sample was heated by the laser.

3.4 Laser profile

Samples were irradiated with the laser to measure and analyze local crystal growth. In Figure 4, a schematic of the laser beam profile and an example image of a measurement is shown. The laser beam has a circular nature however as the laser hits the sample at an angle, the resulting profile of the laser beam when it hits the sample is elliptical. Since crystal growth is induced by temperature, crystals can only grow in those areas in which the temperature is sufficiently high. Due to the laser beam profile the resulting crystals will grow in an elliptical shape, which is clearly seen in the right image. In the image on the right, multiple crystalline (light gray) spots are visible. Each mark indicates a separate measurement on the same sample. From this image it can be seen that the laser only has a local influence, i.e. the material is only heated at the spot where the laser hits the sample.

Because of the crystal shape the crystal growth rate is analyzed across the long axis of the crystal using the line profile analysis as described above. Since the intensity of the laser beam decreases further away from the center of the crystal, only the center part of the crystal is used to determine the crystal growth. The final value is determined by averaging the growth rate on the left and the right side of the crystal.

Laser spot size Previously low-intensity laser measurements were performed. These measurements were done with the same laser with a larger spot size, $1000\ \mu\text{m} \times 440\ \mu\text{m}$ elliptical spot. This research project extends on these measurements by focusing the laser spot to the previously mentioned size of $250\ \mu\text{m} \times 110\ \mu\text{m}$. This increases the intensity of the laser and thus enables us to reach higher temperature regions.

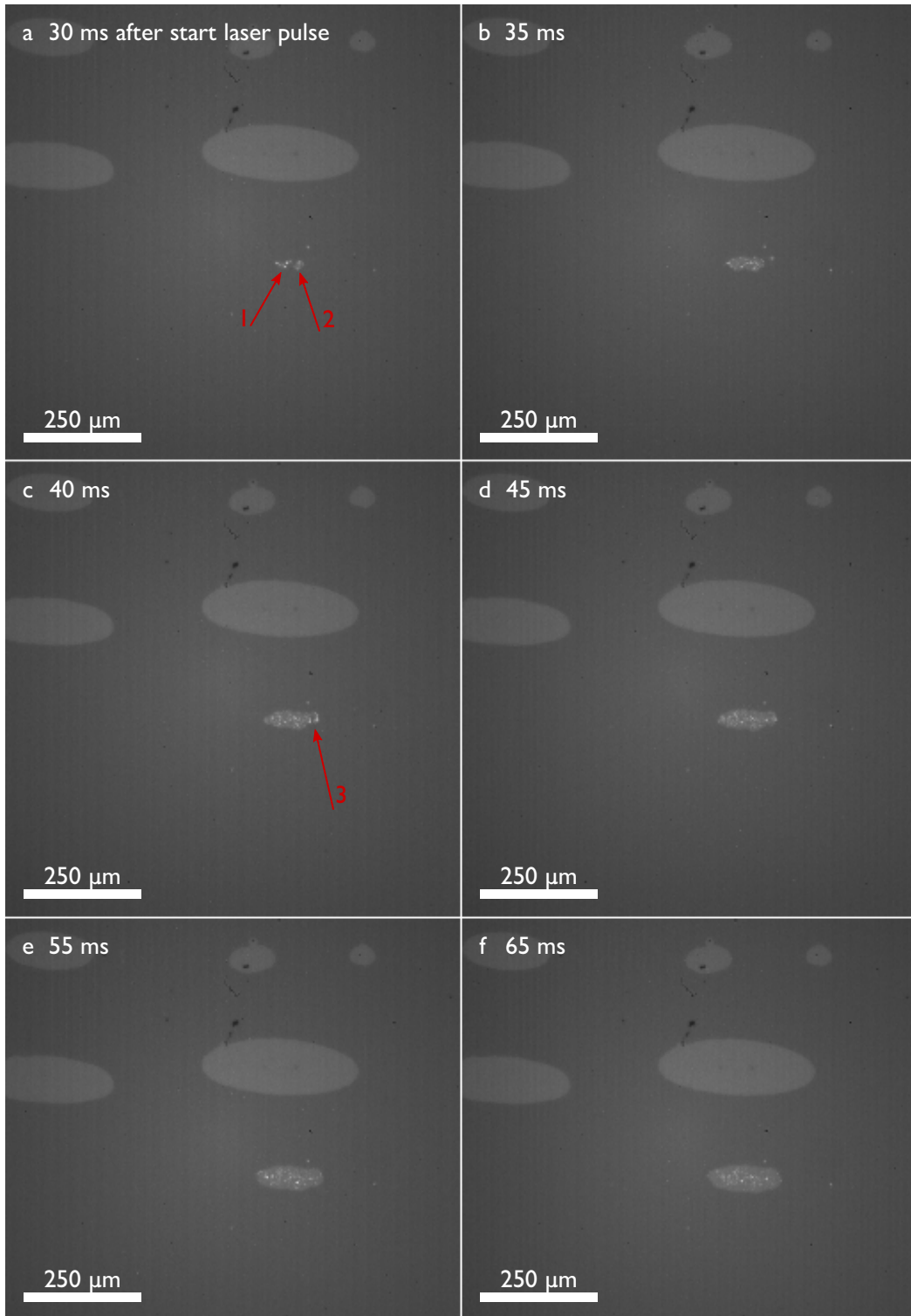


Figure 5: Laser measurement done with $\text{Ge}_8\text{Sb}_{92}$ with a laser power of 90 mW. The laser is switched on at $t = 0$ ms and the images depict the first 65 ms of the measurement. The total measurement took 1400 ms. A clear distinction between nucleation and growth can be made. After a short incubation time, 30 ms, the first crystals nucleate, given by 1 and 2 in **a**. 10 ms later, **c**, a third crystal nucleates. After this no more nucleation is observed, the crystal solely grows. The size of the final crystal is shown in Figure 4

3.5 Analysis of laser induced growth rate profile

As is seen from Equation 7, the growth rate is only dependent on temperature and not on time. Therefore it is expected that for isothermal growth, the growth rate is constant. This is seen in Figure 3h. For the laser induced crystal growth however, due to the Gaussian beam profile the laser intensity over the whole beam profile is not constant and therefore the crystal growth rate is not expected to be constant. The analysis of a measurement on $\text{Ge}_8\text{Sb}_{92}$ with a 90 mW laser beam is shown in Figure 5 and Figure 6. The sample was irradiated for 1.4 s and the images were captured with the high speed camera with 1000 frames per second. In Figure 5, 6 images depicting the first 65 ms after the laser was switched on, are shown. After an incubation time of 30 ms the first crystal nucleate and start to grow outwards, Figure 5a. 10 ms later, Figure 5c, a third crystal nucleates just outside the already existing crystal contributing to the total crystal size. From that point on, no nucleation occurs anymore and the crystal size increases solely due to crystal growth. The final crystal size is depicted in Figure 4.

To analyze the growth rate a coarse and a detailed analysis are performed, Figure 6. For the coarse analysis, the crystal size and the crystal interface position are analyzed every 5 ms for the whole measurement. For the detailed analysis only the first 65 ms are concerned and the crystal size and crystal interface position is analyzed every frame, 1 ms per frame. From the left part of Figure 6 it is seen that the slope of the graph varies depending on the position on the line indicating a varying growth rate dependent on the position along the line. Observing that an increasing slope indicates a decreasing growth rate, the lowest growth rates are found at the edges of the crystal. The highest crystal growth rates are found in the middle of the crystal. This is expected when considering the Gaussian laser beam profile.

The crystal growth rate corresponding to this measurement is the growth rate found at the center of the crystal, i.e. the maximum growth rate. Therefore the beginning of the measurement is analyzed in detail. From the growth map, top image, the position at which nucleation occurred is easily seen. If a crystal originated from a single spot, only ever increasing rings around the center would be observed. In the case where nucleation occurred at multiple spots, multiple of these epicenters should be seen. From the upper right image of Figure 6 multiple of these epicenters are seen. For the line along which the crystal is analyzed, three of these epicenters are observed, corresponding to the three nucleation points indicated in Figure 5. The growth rate is calculated for four regions where local linear behavior is observed. The corresponding growth rates are also given. At the center of the crystal growth rates of $2773 \mu\text{m s}^{-1}$ and $1527 \mu\text{m s}^{-1}$ are found. Averaging the left and right side of the crystal a growth rate of $2150 \mu\text{m s}^{-1}$ is found.

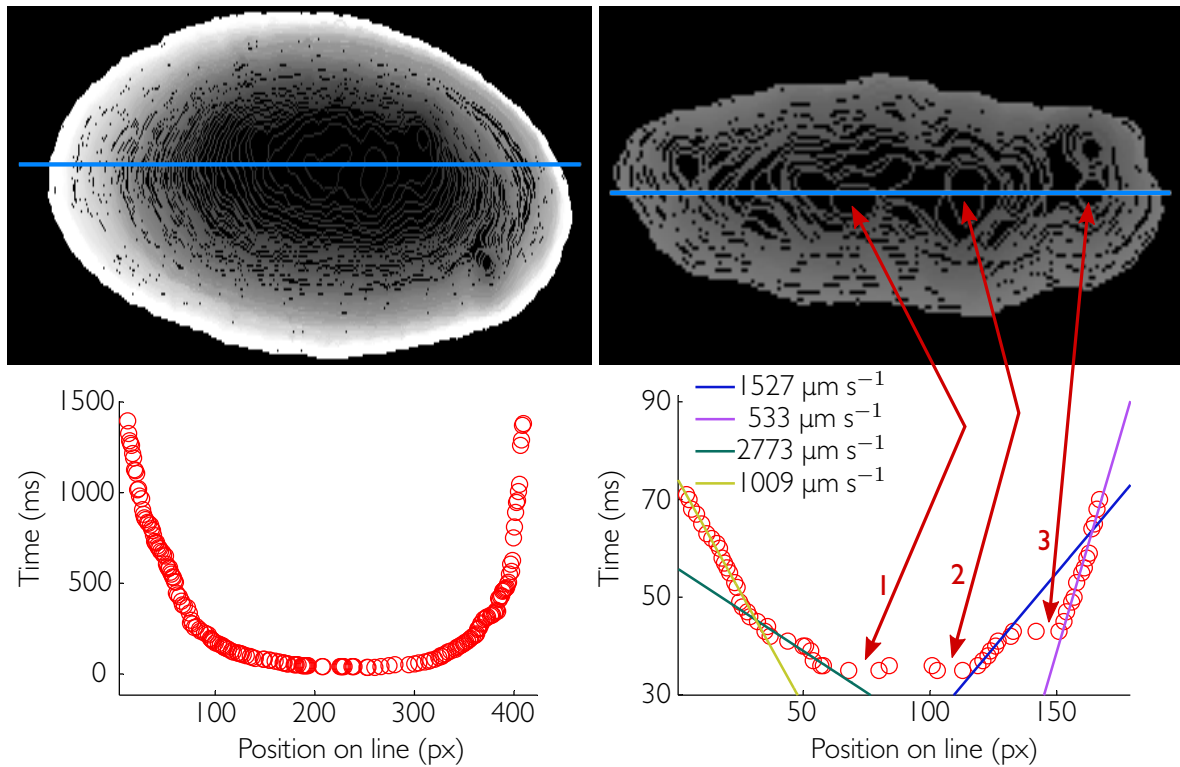


Figure 6: The analysis of the measurement on $\text{Ge}_8\text{Sb}_{92}$ with a 90 mW laser beam, depicted in Figure 5. The growth speed is analyzed via a line profile analysis. **(left)** The full measurement is analyzed along the depicted blue line. Every 5 ms the crystal size and the position of the interface is analyzed. Further away from the center of the crystal the temperature decreases and therefore the crystal growth rate decreases. **(right)** To improve on the accuracy of the analysis, the crystal is analyzed in detail for the first 65 ms along the blue line. Now every 1 ms the crystal size and the position of the interface is analyzed. In the analysis the difference between nucleation and growth is seen clearly. The arrows indicate the position in the crystal where nucleation occurred with the corresponding position in the graph. The numbers in the graph correspond with the numbers in Figure 5. In four areas the growth rate is analyzed. As is expected the growth rate is highest, closest to the center of the crystal, and diminishes further away from the center.

4 Results and discussions

The crystal growth rate in $\text{Ge}_x\text{Sb}_{1-x}$ with compositions $x = 6, 7, 8, 9, 10$, is measured. Crystal growth is a temperature activated process, where higher temperatures lead to higher growth rates. By using a laser to irradiate the samples, it is possible to measure the crystal growth rate in a temperature region significantly higher than what was previously attainable with isothermal measurements. The isothermal measurements involve heating the whole sample and analyzing the growth rate of the various crystals. In this case the whole sample can only be used once. When using the laser, the sample is first heated to an as high as possible temperature, where the growth rate is still very small. The laser then heats the local area to higher temperatures. Since only the local area is crystallized, many measurements can be done on one sample. In this analysis the measured growth rate will be used to determine the local temperature conditions when the sample is irradiated by the laser.

4.1 Crystal growth rate in the high temperature domain

In Figure 7a the crystal growth rate is plotted versus $1/k_bT$ on a logarithmic scale for the isothermal measurements as obtained by Gert Eising [42]. For all compositions, $\text{Ge}_x\text{Sb}_{1-x}$ with $x = 6, 7, 8, 9, 10$, it is seen that a linear fit describes the measurements very closely which is in agreement with the Arrhenius model of the crystal growth rate, see Equation 1. In Figure 7b the isothermal measurements of $\text{Ge}_6\text{Sb}_{94}$ (blue diamonds) combined with the laser measurements at a stage temperature of 90°C are shown (red squares). It is seen that by increasing the laser power the crystal growth rate drastically increases.

Measuring the local temperature during the laser irradiation directly proved to be very difficult, therefore another method is used to determine the temperature difference induced by the laser. By assuming Arrhenius behavior over the complete temperature interval for $\text{Ge}_6\text{Sb}_{94}$, the corresponding local temperature can be calculated for each measured growth rate. The temperature difference is then simply the difference between this calculated temperature and the stage temperature during the measurement. This is depicted in Figure 7b by the arrow denoting ΔT . This ΔT can then be coupled to that laser power. Using this calibration, the temperature corresponding to the growth rate during measurements for the other compositions can be found. The justification for this reasoning will be explained below.

Now that it is known what the temperature difference is due to the added laser power, we can extend Figure 7a for all the materials. In Figure 8 all the results are gathered, i.e. the isothermal, the large laser spot and the small laser spot results. The new results, the small laser spot results, are indicated above the thin dashed line. The Arrhenius fits are also depicted for comparison reasons. The crystal growth rates during the isothermal measurements are of the order of $1 \mu\text{m s}^{-1}$ where with the laser, growth rates of the order of 20 mm s^{-1} are obtained, about 20000 times faster. By assumption the results for $\text{Ge}_6\text{Sb}_{94}$ do not deviate from the Arrhenius behavior. The $\text{Ge}_7\text{Sb}_{93}$ and $\text{Ge}_8\text{Sb}_{92}$ results initially follow the Arrhenius behavior but at higher temperatures the growth rate becomes lower than expected from the Arrhenius fits. For $\text{Ge}_9\text{Sb}_{91}$ it is observed that this deviation occurs much earlier, already around $10 \mu\text{m s}^{-1}$. Looking at the high temperature region for $\text{Ge}_{10}\text{Sb}_{90}$ the same deviation from the Arrhenius behavior is observed. The change in slope of the logarithm of the growth rate versus reciprocal temperature indicates a temperature dependence of the activation energy for growth.

Using the laser heating measurements of $\text{Ge}_6\text{Sb}_{94}$ as calibration as local temperature estimator The deviation with respect to the Arrhenius fits is expected since it is well established that GeSb alloys with

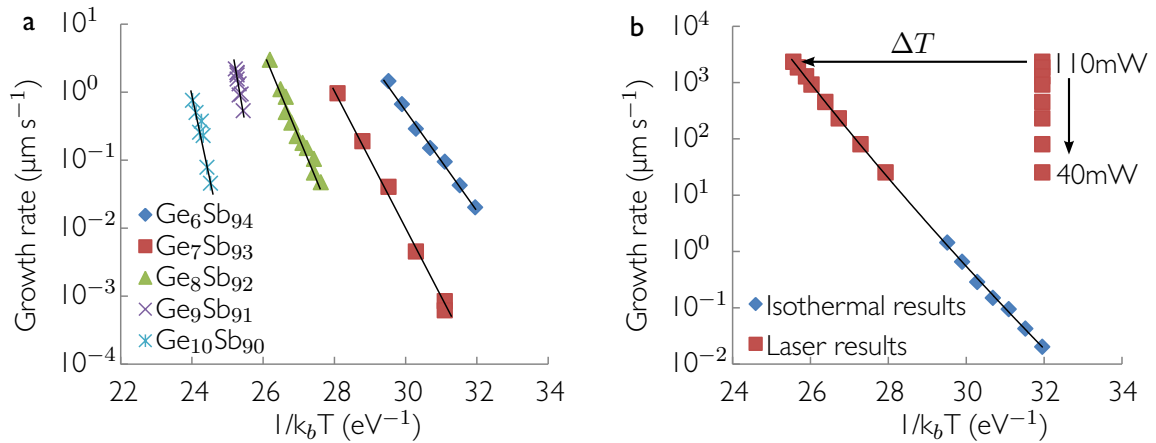


Figure 7: **a)** Crystal growth rate found with isothermal measurements for the $\text{Ge}_x\text{Sb}_{1-x}$ compositions versus the reciprocal temperature. Results obtained by Gert Eising [42]. The linear fit indicates Arrhenius behavior is observed in this low temperature regime for each composition. To extend these graphs in higher temperature regimes, a laser is used. **b)** $\text{Ge}_6\text{Sb}_{94}$ was heated to 90°C , next the sample was irradiated with a laser with a power varying from 40 mW to 110 mW. To determine the temperature increase (ΔT) induced by the laser, Arrhenius behavior is assumed in the high temperature regime. ΔT is then found by calculating the temperature corresponding with the measured growth rate and subtracting the stage temperature (90°C in this case).

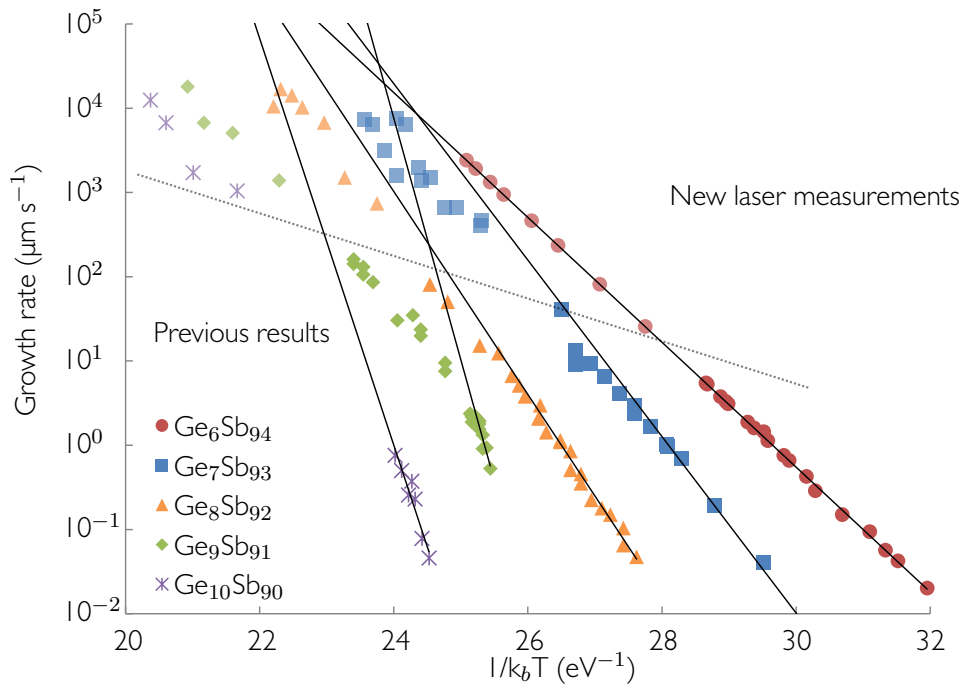


Figure 8: Local crystal growth rates of isothermal measurements and additional laser heating versus the reciprocal temperature for compositions $\text{Ge}_6\text{Sb}_{94}$ to $\text{Ge}_{10}\text{Sb}_{90}$. The region above the dashed line indicates the temperature region which was reached with the additional heating of the smaller laser spot. Below the dashed line the isothermal results are given combined with earlier laser experiments done with a large laser spot. For $\text{Ge}_{10}\text{Sb}_{90}$ no measurements were done with the large laser spot. The Arrhenius fits are identical to the fits in Figure 7a. The local temperature during the measurement of $\text{Ge}_7\text{Sb}_{93}$ to $\text{Ge}_{10}\text{Sb}_{90}$ is determined using the calibration obtained from $\text{Ge}_6\text{Sb}_{94}$. It is seen that in the high temperature regime, the behavior deviates substantially from the Arrhenius behavior.

higher antimony content exhibit higher maximum crystallization rates [45]. For example if the crystallization growth for $\text{Ge}_{10}\text{Sb}_{90}$ would follow the Arrhenius behavior it would reach higher crystallization rates than $\text{Ge}_6\text{Sb}_{94}$ at higher temperatures which would be unexpected. Therefore the slope of the measured growth rate of $\text{Ge}_{10}\text{Sb}_{90}$ has to decrease at higher temperatures (when compared to the Arrhenius plot extrapolated beyond the isothermal results) such that the growth rates remain below the growth rates of $\text{Ge}_9\text{Sb}_{91}$, which in turn have to remain below the growth rates of $\text{Ge}_8\text{Sb}_{92}$ and so on. By using the calibration obtained from the measurements with $\text{Ge}_6\text{Sb}_{94}$ it is indeed seen in Figure 8 that this constraint is upheld. In this way $\text{Ge}_9\text{Sb}_{91}$ and $\text{Ge}_{10}\text{Sb}_{90}$ show most pronounced non-Arrhenius behavior whereas $\text{Ge}_6\text{Sb}_{94}$ has to show most pronounced Arrhenius behavior. This is the justification for making the explicit assumption that $\text{Ge}_6\text{Sb}_{94}$ keeps its Arrhenius behavior during laser heating. The combined results of Figure 8 for the various GeSb compositions together with the known increase in maximum crystallization speed with decreasing Ge-concentration (see e.g. ref [45]) show that there is in fact no alternative solution, i.e. most pronounced Arrhenius behavior for $\text{Ge}_6\text{Sb}_{94}$ and most pronounced non-Arrhenius behavior for $\text{Ge}_{10}\text{Sb}_{90}$. Recently it has been shown that the crystal growth rate for the AgInSbTe phase-change material follows strict Arrhenius behavior over eight orders of magnitude, from $\sim 10 \text{ nm s}^{-1}$ to $\sim 1 \text{ m s}^{-1}$ [39]. Since AgInSbTe is also a well-known fast-growth-type PCM like the GeSb-alloys used here, it is certainly appears possible that $\text{Ge}_6\text{Sb}_{94}$ follows strict Arrhenius behavior over four orders of magnitude, $\sim 100 \text{ nm s}^{-1}$ to $\sim 1 \text{ mm s}^{-1}$.

4.2 Influence of experimental parameters on added laser heat

Stage temperature influence Although the calibration based on $\text{Ge}_6\text{Sb}_{94}$, see Figure 7, yields plausible results, it is still an estimation. From other results it is seen that both the stage temperature at which the measurement starts and the composition of the sample play an important role in the resulting crystal growth rate and thus the heat which is added to the sample. Extensive measurements were done on $\text{Ge}_8\text{Sb}_{92}$ to determine the influence of the stage temperature on the resulting added heat due to the laser beam. In Figure 9 the temperature difference induced by the laser is plotted versus the laser power at a given stage temperature and versus the stage temperature at a given laser power. Since the composition is an important factor we want to confine ourselves to the composition at hand, $\text{Ge}_8\text{Sb}_{92}$. Therefore, the temperature increase was determined by using the Arrhenius fit of $\text{Ge}_8\text{Sb}_{92}$ using the same method as described in Figure 7. From Figure 9 it is clearly seen that increasing the stage temperature reduces the effect of the laser. This could be explained as follows: Due to increased energy losses, more energy is needed to heat an object from 160°C to 180°C than to heat that same object from 150°C to 170°C . By assuming that a given laser power will add the same amount of energy whatever the temperature of the object, less net heat will be added if the initial stage temperature is higher. Another observed effect is that increasing the laser power yields diminishing returns. Actually, this is exactly what is expected because a higher temperature difference between the laser-irradiated area and the surrounding area results in more heat loss to the surroundings. Therefore it is expected that the returns diminish as the laser power is increased. Because the calibration based on $\text{Ge}_6\text{Sb}_{94}$ was done with measurements performed at 90°C , while measurements with the other compositions were conducted at much higher temperatures, this calibration can be seen as a upper boundary of the actual temperature increase.

Composition influence Still it is not fully understood what the effect of the laser is for different compositions. In Figure 10 the temperature difference versus the laser power is plotted for all compositions. The temperature for each composition is determined with respect to the corresponding Arrhenius fits for each composition as in Figure 7. Where we would expect the added heat of the laser to be most for

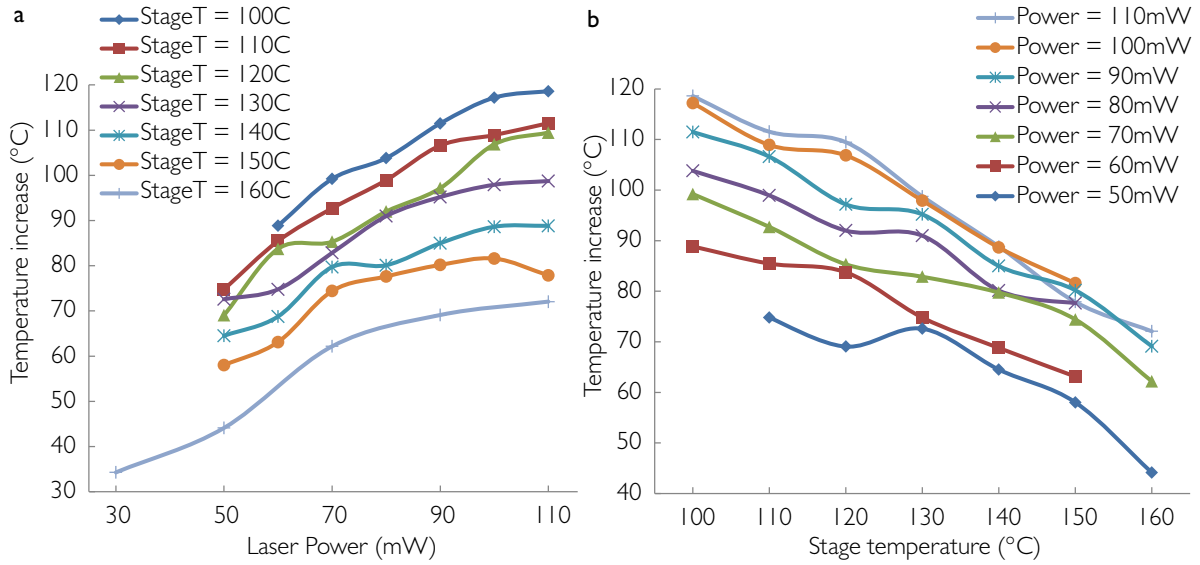


Figure 9: **a)** Temperature increase versus laser power for $\text{Ge}_8\text{Sb}_{92}$ at different stage temperatures. **b)** Temperature increase versus stage temperature for $\text{Ge}_8\text{Sb}_{92}$ at different laser powers. The interpolation between the data points is meant as guidance for the eye. Temperature differences were determined using the Arrhenius fit of $\text{Ge}_8\text{Sb}_{92}$ instead of $\text{Ge}_6\text{Sb}_{94}$ as calibration, see Figure 7. At a given stage temperature it can be seen that the effect of additional laser power decreases as the laser power increases. At a given laser power it can be seen that less heat is added by the laser as the stage temperature increases.

the lowest temperature, 90°C $\text{Ge}_6\text{Sb}_{94}$, we see that for 100°C $\text{Ge}_8\text{Sb}_{92}$ the temperature difference is already $\sim 20^\circ\text{C}$ higher everywhere. A possible explanation for the results could be found in the coupling of the laser light with the sample surface. The Brewster's angle is chosen such that there is no reflection. The angle is calculated based on the refractive index of $\text{Ge}_{10}\text{Sb}_{90}$ for the given wavelength of the laser light [43]. Since the refractive index can vary between the different compositions, the coupling of the laser light with the sample surface can vary as well. From Figure 10 it is seen that higher germanium content compositions have a higher temperature difference for comparable temperatures than lower germanium content compositions, which could indicate that the closer the composition is to $\text{Ge}_{10}\text{Sb}_{90}$, the better the coupling between the laser light and the surface is.

With these extra conclusions the justification for the calibration with $\text{Ge}_6\text{Sb}_{94}$ can be strengthened further. While it is true that for higher germanium content composition the coupling seems better and therefore the effect of the laser seems larger, the calibration was done at lower temperatures. It is seen from Figure 10 that the temperature differences of the $\text{Ge}_6\text{Sb}_{94}$ measurement at 90°C are still higher than those for the other compositions at higher temperatures. Combining the facts that higher stage temperature means lower added heat, and that higher germanium content means better coupling together with the fact that we expect deviation from the Arrhenius behavior for the higher germanium content compositions (and we see this deviation happening with our calibration), we see that the calibration is a plausible upper boundary.

4.3 Viscosity model

Now that the results for the measurements have been established, it is interesting to extrapolate the crystal growth rate to higher temperatures, such that a maximum crystal growth rate can be obtained. To

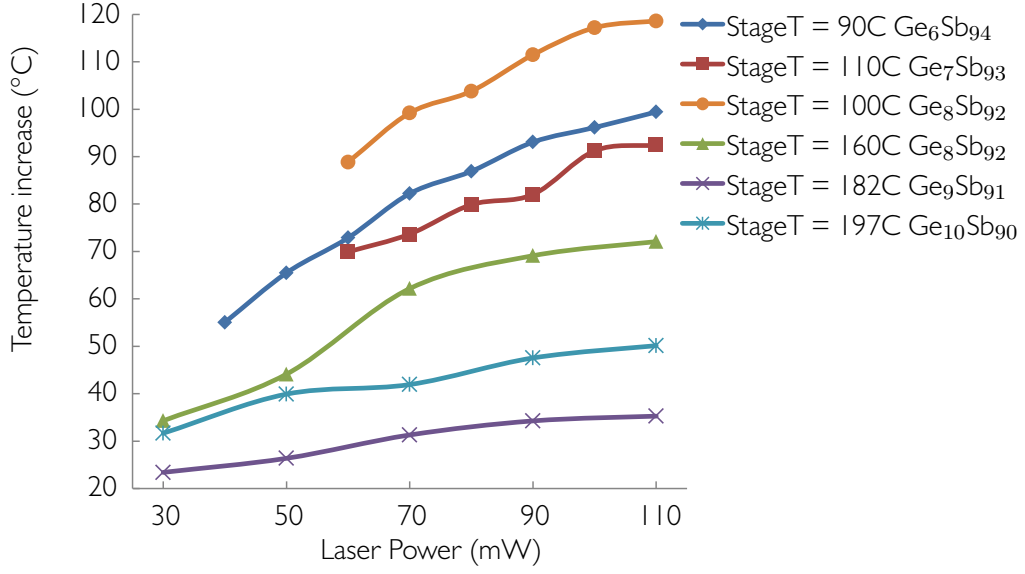


Figure 10: Temperature increase versus laser power for the different composition. The measurements were chosen based on the lowest stage temperature at which measurements were done for each composition. The interpolation between the data points is meant as guidance for the eye. Here it is seen that the effect of the laser differs a lot depending on the composition. Compositions with higher germanium content have more heat added than those with lower germanium content for comparable temperatures.

	Ge ₆ Sb ₉₄	Ge ₇ Sb ₉₃	Ge ₈ Sb ₉₂	Ge ₉ Sb ₉₁	Ge ₁₀ Sb ₉₀
T_m (K)	887.72	885.05	882.37	879.70	877.03
$1/k_b T$ (eV ⁻¹)	13.07	13.11	13.15	13.19	13.23

Table 1: Melting temperature of different compositions.

extrapolate the results, the viscosity of the material during crystallization is calculated using Equation 12. Then the VFT, Equation 10, and Mauro models, Equation 11 are fitted to the data. The models are then used to calculate the crystal growth rate at high temperatures. The values used for the calculation are: $R_{\text{hyd}} \sim 0.5 \text{ \AA}$, $r_{\text{atom}} \sim 1.5 \text{ \AA}$, $\lambda \sim 1 \text{ \AA}$, these values are based on the values reported for AgInSbTe [39] and $\Delta H_m \sim 0.22 \text{ eV at}^{-1}$ [46]. The melting temperatures for the different compositions are given in Table 1. [47]

The three fitting parameters in both models are the viscosity at infinite temperature, η_∞ , the glass temperature, T_g , and the fragility m . In ref [38] it is argued that in the limit of infinite temperature the viscosity for one particular class of materials should be universal. Namely at infinite temperature, the details of the interatomic potentials are no longer important because the system is dominated by kinetic energy. From their analysis the value $\eta_\infty = -3$ is chosen. In Table 2, the results of the fitting are given and in Figure 11 the viscosity is plotted versus the reciprocal temperature up to the melting temperature. Values for Ge₆Sb₉₄ are also shown. These were obtained by not assuming Arrhenius behavior anymore and directly fit the models to the data points as is done for the other compositions. It is seen that for both models the viscosity is about the same for the different compositions at the melting temperature. The VFT model consequently estimates higher values of the fragility and the glass temperature when compared to the Mauro model. Literature values for the glass transition temperature of the used compositions are not found, although for Ge₁₂Sb₈₈ a value of $T_g \sim 466 \text{ K}$ is reported. Comparing the found results with this

		Ge ₆ Sb ₉₄	Ge ₇ Sb ₉₃	Ge ₈ Sb ₉₂	Ge ₉ Sb ₉₁	Ge ₁₀ Sb ₉₀
Mauro	T_g (K)	324	352	382	395	430
	m	46	54	62	58	68
	Max growth rate (m s ⁻¹)	6.0	9.7	13.7	6.5	8.7
VFT	T_g (K)	331	357	392	409	443
	m	60	71	92	91	109
	Max growth rate (m s ⁻¹)	2.1	2.4	3.2	2.1	2.2

Table 2: Fragility, glass temperature and maximum growth speed obtained from fitting the both the Mauro and the VFT model to the data points. $\eta_\infty = -3$ is fixed. The data points for Ge₆Sb₉₄ were obtained by not assuming Arrhenius behavior anymore.

value it is seen that the results of both models are plausible.

In Figure 12 the crystal growth rate extrapolation as calculated from the viscosity versus the reciprocal temperature is shown. Again the crystal growth rate is plotted up to the melting temperature. In Table 2 the maximum crystal growth rate for each composition is shown. It is seen that the maximum growth rate is about same for both models, ~ 2 m s⁻¹ for the VFT model and ~ 10 m s⁻¹ for the Mauro model, where the Mauro model consequently predicts higher growth rates. In Figure 14 the maximum growth rate versus the germanium content of Ge_xSb_{1-x} alloys is plotted, adapted from ref [45]. Here it is seen that by decreasing the germanium content in the alloys, the maximum measured growth speed drastically increases. A prudent extrapolation has been made in Figure 14. If this relation would hold for the compositions studied here, much higher maximum growth rate than 58 m s⁻¹ are expected to be found. It is clear from Table 2 that these higher growth rates are not found. The experiments done in ref [45] where however performed on melt-quenched films, whereas the experiments done here were performed on as-deposited films. In earlier research it has been shown that a temperature shift is expected when going from as-deposited films to melt-quenched films. For example a decrease of 42 K for Ge₁₅Sb₈₅ has been reported. [48] Earlier work done by Jasper Oosthoek [49] for Ge and In doped SbTe alloys also showed that the same crystal growth rate for melt-quenched materials occurred at temperatures about 25 K lower than for as-deposited materials.

For phase-change material applications in for example DVD rewritable's it is desired to have a high crystallization rate at writing temperatures but have low crystallization rates at operating conditions, such that spontaneous crystallization does not occur. Phase-change material based devices should be able to retain their state for at least 10 years. If a rectangular cell has a width of 100 nm and the crystal grows from the edges towards the center, the crystal has to grow over 50 nm. The growth rate at operating temperatures then has to be smaller than $\sim 1.59 \cdot 10^{-16}$ m s⁻¹ such that the state of the cell can be retained over 10 years. From Figure 12 this retention point is found. The values are given in Table 3. If the maximum operating temperature is about 100°C it is seen that compositions Ge₈Sb₉₂, Ge₉Sb₉₁ and Ge₁₀Sb₉₀ best meet this requirement.

When for the VFT model η_∞ is not fixed at -3, unphysical results are obtained. The corresponding viscosity and extrapolated crystal growth are given in Figure 13. It is seen that growth rates of ~ 10 km s⁻¹ and $\eta_\infty \sim -10$ for Ge₇Sb₉₃ and Ge₈Sb₉₂ are found, which are very unrealistic values. This result strengthens our choice to fix the value of η_∞ during the fitting.

The results put in perspective The ideal phase-change material exhibits zero to no crystal growth at operating temperatures and below, and maximum growth at elevated temperatures. The first case

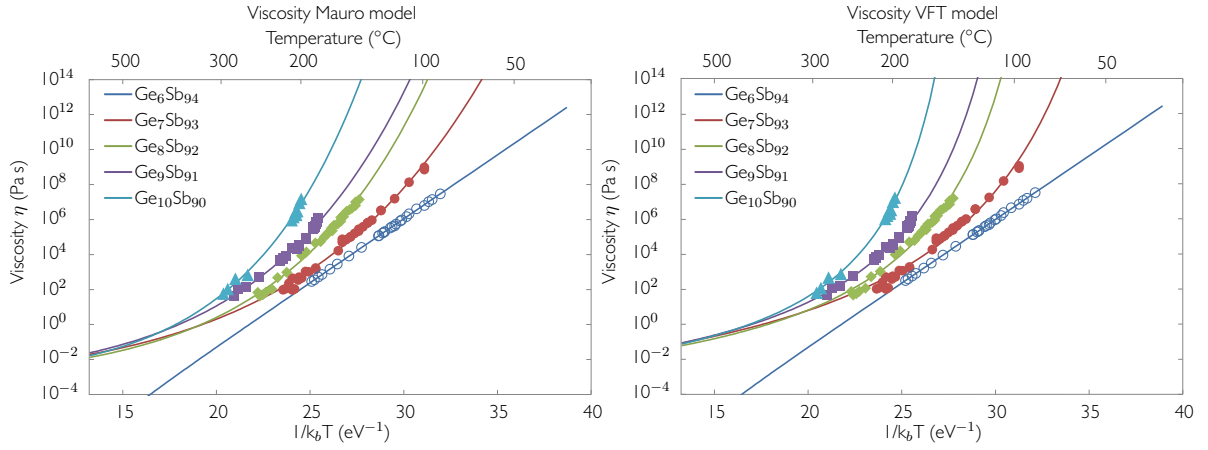


Figure 11: Mauro (left) and VFT (right) viscosity models plotted as function of the reciprocal temperature up to the melting temperature for all compositions. The glass temperature and fragility for each composition and each model is given in Table 2. For $\text{Ge}_6\text{Sb}_{94}$ Arrhenius behavior is assumed and a straight line is plotted correspondingly.

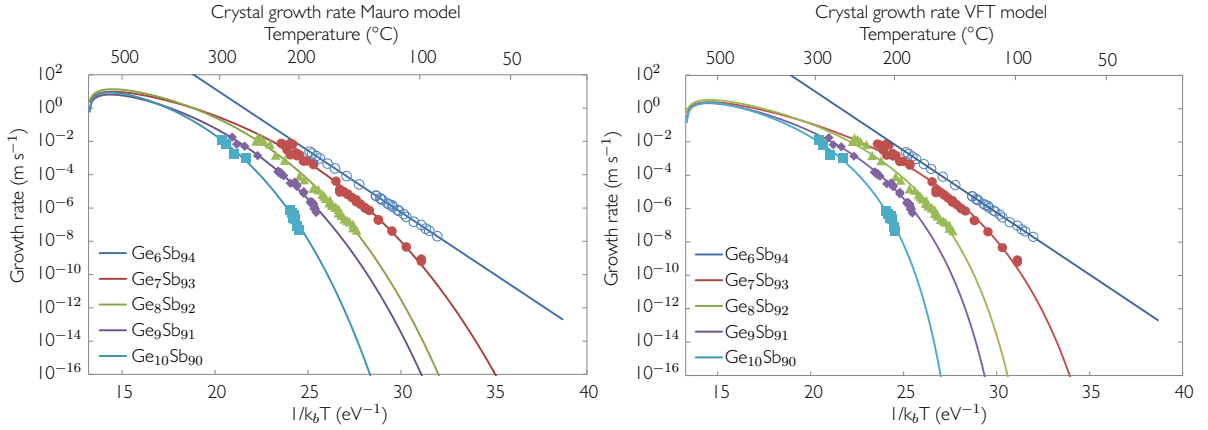


Figure 12: Crystal growth rate as calculated from the obtained viscosity fits using Equation 12 for all compositions. The maximum growth speed derived from both models is given in Table 2. The difference between the models is small and consequently similar results are obtained. It is also seen that $\text{Ge}_6\text{Sb}_{94}$ cannot follow Arrhenius behavior indefinitely, as this would result in unrealistically high growth rates close to the melting temperature.

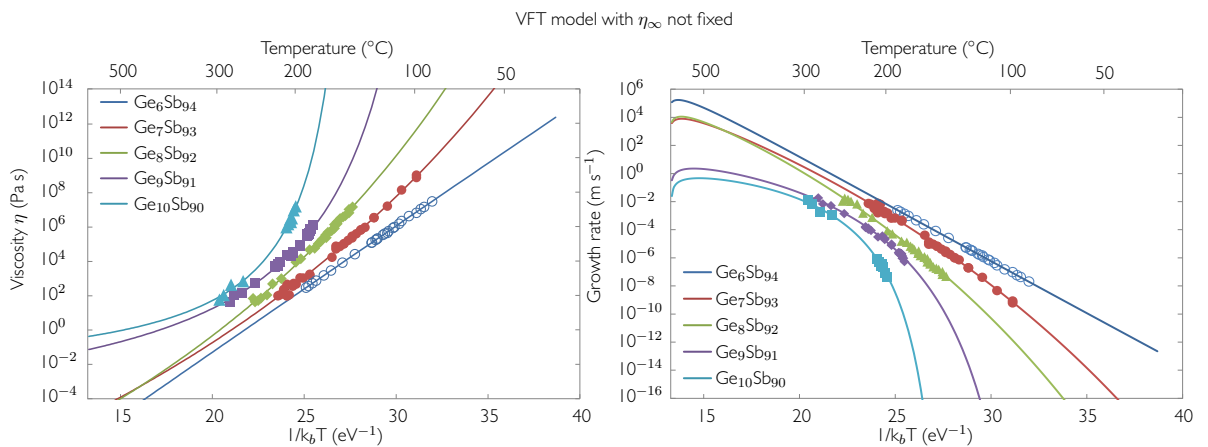


Figure 13: When η_∞ is not fixed in the VFT model, the results become unphysical, i.e. maximum growth rate $\sim 10 \text{ km s}^{-1}$ and $\eta_\infty \sim -10$.

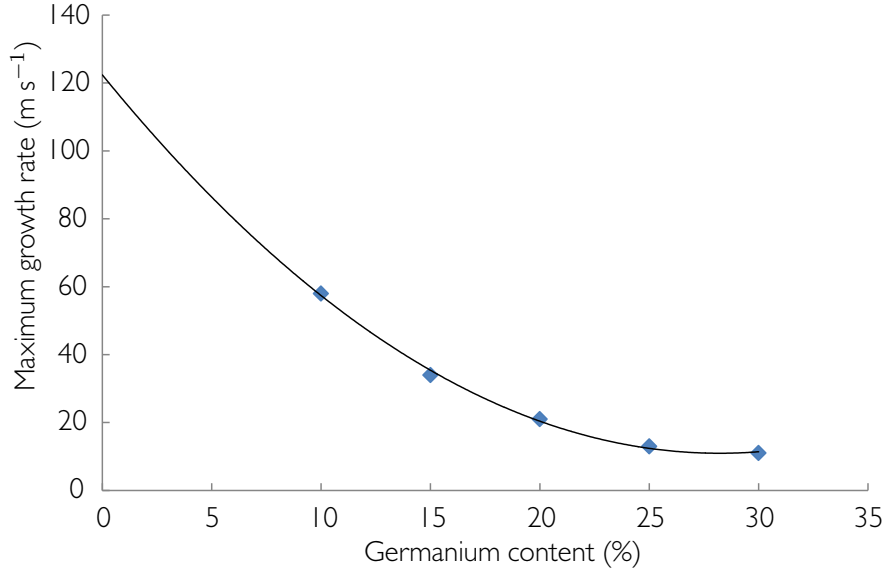


Figure 14: Maximum crystal growth rate of $\text{Ge}_x\text{Sb}_{1-x}$ alloys versus the germanium content as reported in ref [45]. For $\text{Ge}_{10}\text{Sb}_{90}$ it is seen that a maximum growth rate of 58 m s^{-1} is found. A prudent extrapolation indicates that maximum growth rate for the compositions studied here is expected to be much higher than 58 m s^{-1} .

$T_{\text{ret}}(^{\circ}\text{C})$	$\text{Ge}_6\text{Sb}_{94}$	$\text{Ge}_7\text{Sb}_{93}$	$\text{Ge}_8\text{Sb}_{92}$	$\text{Ge}_9\text{Sb}_{91}$	$\text{Ge}_{10}\text{Sb}_{90}$
Arrhenius	-2				
Mauro		58	89	100	138
VFT		68	107	122	157

Table 3: Maximum operating temperature, $T_{\text{ret}}(^{\circ}\text{C})$, at which a 100 nm rectangular data cell in for example a DVD rewritable still retains its data integrity after 10 years for all compositions. For $\text{Ge}_6\text{Sb}_{94}$ the retention point is calculated from the assumed Arrhenius behavior.

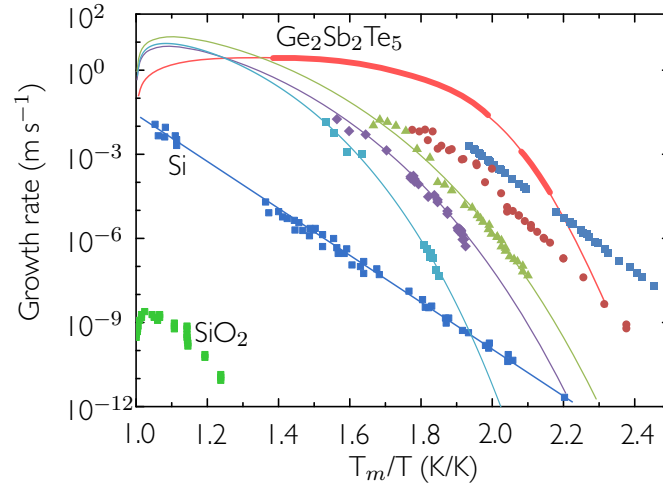


Figure 15: Crystal growth rates of $\text{Ge}_2\text{Sb}_2\text{Te}_5$, Si and SiO_2 compared with the obtained results from this research. The newly obtained results are depicted in similar fashion as in previous Figures, for example Figure 12. It is seen that Si shows perfect Arrhenius behavior over the full temperature range whereas $\text{Ge}_2\text{Sb}_2\text{Te}_5$ and the GeSb alloys show pronounced fragile behavior. The studied alloys show a lower crystal growth rate at lower temperatures but show a higher maximum crystal growth rate, indicating better performance than $\text{Ge}_2\text{Sb}_2\text{Te}_5$. The data for $\text{Ge}_2\text{Sb}_2\text{Te}_5$, Si and SiO_2 is adapted from ref [18]

is to ensure that at storing and operating conditions the data is preserved indefinitely and the second case ensures that the performance does not vary much with varying temperature (when considering many write cycles, a laser beam will not always exhibit the same intensity each cycle, correspondingly the local induced temperature can vary as well. This should not hamper the resulting crystal growth rate however). In real life such behavior is not possible, although fragile materials best approximate this behavior. Therefore fragility is a useful indicator when considering the relevance of an alloy. In Figure 15 the obtained results are compared with results obtained for other alloys as described in ref [18]. Both the results from ref [18] as well as the results from this report hold for as-deposited films. It is seen that Si shows Arrhenius behavior over the full temperature range whereas $\text{Ge}_2\text{Sb}_2\text{Te}_5$ and the GeSb alloys show fragile behavior, except for $\text{Ge}_6\text{Sb}_{94}$ for which Arrhenius behavior is assumed. It is seen that at lower temperatures the GeSb alloys have lower crystal growth rates, which is useful when concerning the ability to retain data, and have higher crystal growth rates at higher temperatures than $\text{Ge}_2\text{Sb}_2\text{Te}_5$. Thus the GeSb alloys show improved performance over $\text{Ge}_2\text{Sb}_2\text{Te}_5$. However, Figure 15 does not show the full picture. GeSb alloys are for example more prone to phase separation, thus cell endurance is clearly more an issue for the studied materials. Also as mentioned before, there is a clear difference between the temperature dependent crystal growth of as-deposited films and melt-quenched films. Further research is therefore necessary to unravel the complete behavior of GeSb alloys.

5 Other work

5.1 Gold nanorods and surface plasmons

In the progress of increasing the crystal growth rate of the GeSb alloys an interesting side track was briefly explored. In ref [50] an experiment is described where a water solution with mixed in gold nanoparticles is irradiated with sunlight. It is observed that steam is generated due to the presence of the nanoparticles. Namely subwavelength metallic particles are intense absorbers of optical radiation due to the collective oscillations of their delocalized conduction electrons, also known as surface plasmons. When the particles are excited at their resonance frequency, the energy which is not reradiated through light scattering is dissipated through Landau (non-radiative) damping [51]. The Landau damping causes a dramatic rise in temperature in the nanometer-scale vicinity of the particle surface. It is still unclear what the complete behavior behind this phenomenon is although attempts have been made to get a better understanding of the physics. [52–55]

In the case of the described experiment the immersed nanoparticles heated the local water around the nanoparticles, evaporating it and creating little vapor bubbles around the nanoparticle. After the bubble had grown sufficiently, it would rise to the vapor-air interface where it would release the vapor. The nanoparticle is then immersed into the water again to repeat the process. An interesting aspect to this phenomenon is that the steam and thus the heat is produced almost instantaneously.

This leads to the question whether combining these nanoparticles with phase-change material will lead to increased crystal growth when irradiated with optical radiation. To this end we acquired gold nanorods which have their resonance frequency around the wavelength of our laser. The nanorods were supplied by Sigma-Aldrich, product number 771686, and have width between 22.5-27.5 nm and length between 54-66 nm resulting in a resonance peak around a wavelength of 625-675 nm. To prevent the nanorods from clotting, cetrimonium bromide (CTAB) is added to the solution as stabilizer. As phase-change material Ge₈Sb₉₂ is used. The nanoparticles were first solved in water which was then dispensed on the surface of the PCM.

SEM images In Figure 16, SEM images are shown of the dispensed drop after the water was evaporated. In Figure 16a the full drop is depicted. The black circle is the edge of the drop while the large dark gray areas are landmarks which help locating possible interesting areas. It is seen that there is a large group of white speckles at the center of the drop. A zoomed image of the center is seen in Figure 16b. Considering the size of the squares, these cannot be the nanoparticles, rather it is found that the squares are the stabilizer molecules in crystallized form. It is further observed that almost no nanoparticles are found at the center. Zooming in at the edge of the drop, Figure 16c, we see a very different configuration. Instead of squares, spike shapes are seen. Zooming in even further, Figure 16d, we see that these spiked shapes are in fact clusters of nanoparticles. Here it is clearly seen that the nanoparticles are cylindrical in shape. In between the edge and the center of the drop, almost nothing is observed. Thus the nanoparticles are concentrated in clusters at the edge of the drop while the stabilizer crystallized in the center of the drop. A poor distribution of nanoparticles is therefore achieved with this dispersion method.

Growth rate In Figure 17 the same image as Figure 16a is shown except here it is taken by the optical camera. The areas where crystals were grown are now clearly visible. To test the influence of the nanoparticles on the growth behavior, measurements were done at various locations, i.e. at the edge of

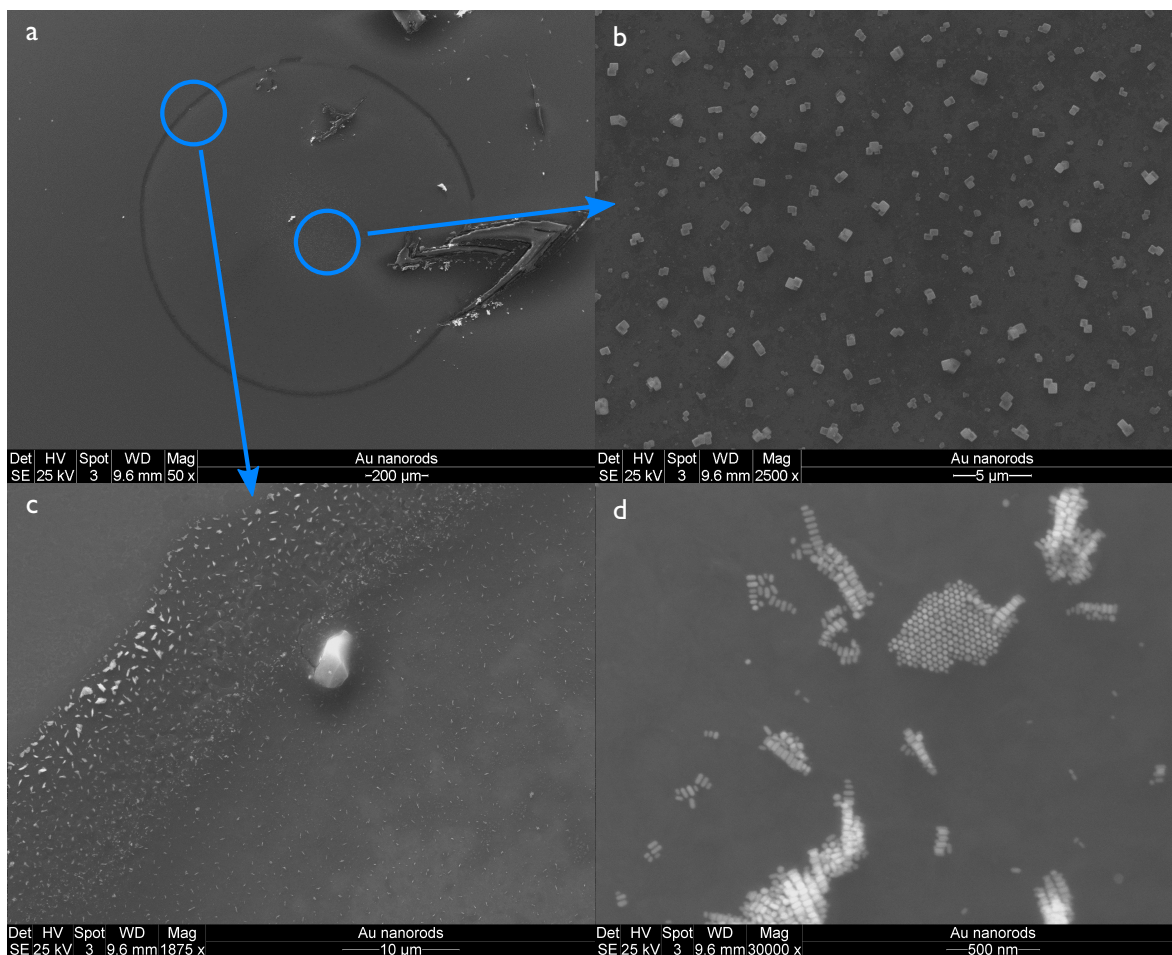


Figure 16: SEM images of dispensed nanoparticle on a $\text{Ge}_8\text{Sb}_{92}$ sample. **a** Image of the full drop. The black circle indicates the edge of the drop, the large dark gray marks are made as landscape marks to easily locate possible interesting areas. Two areas of interested are inspected each indicated with a blue circle. **b** Zoomed view of the center of the circle. The blocks visible are the stabilizer in crystallized form. Almost no nanoparticles are found at the center of the drop. **c** Zoomed view of the edge of the drop. The small white speckles are all nanoparticles. At the edge no stabilizer is found. **d** Further zoom of the nanoparticles as found in image **c**. The particles are found in neat grids either in upright orientation or in sideways orientation. Here is seen very clearly that the nanoparticles are cylindrical in shape. The images were taken by Gert ten Brink

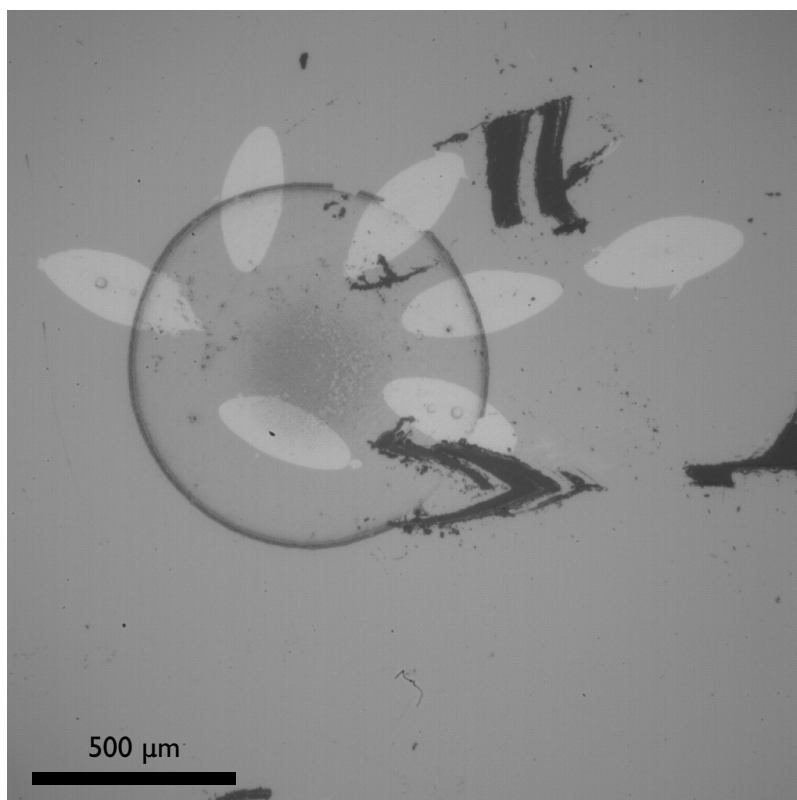


Figure 17: Same image as Figure 16 but taken with the optical camera. The landmarks can be used to compare the two images. The sample, $\text{Ge}_8\text{Sb}_{92}$, was preheated to 140°C and then irradiated with a 80 mW laser beam in different locations to determine the influence of the nanoparticles on the growth behavior. It is seen that the crystal on the edge of the drop do not differ significantly in size from the crystal in the center of the drop and the crystal outside the drop.

the drop, at the center of the drop and outside the drop. This three areas are characterized as a nanoparticle rich area, a crystallized stabilizer rich area and a non-enhanced area respectively. The crystals were grown by irradiating the sample which was preheated to 140°C with a 80 mW laser beam. Judging from the crystal sizes, no significant difference in final crystal size between the different areas is observed.

The growth rate could not be studied very accurately. Due to the presence of the nanoparticles and stabilizer molecules the light of the laser beam was reflected very strongly. As this reflection occurred in the region in which the crystal grows it was difficult to accurately assess the crystal growth rate. The attempts done to measure the growth rate indicate varying growth rates from which no significantly distinguishable effect could be attributed due to the presence of the nanoparticles. In Figure 18 the reflection of the laser beam is also seen as the white stains in the picture. Here it is clearly seen that these stains obscure the area of the sample below, making it impossible to see the crystal-amorphous interface there.

However some interesting effects were sometimes observed. In Figure 18 part of a measurement is shown in which a deviation of normal behavior is observed. Suddenly, for a brief period of 25 ms, the crystal growth rate accelerates drastically. The growth rate accelerates from $180 \mu\text{m s}^{-1}$ to $2254 \mu\text{m s}^{-1}$ to decrease back to $43 \mu\text{m s}^{-1}$ afterwards. The cause for this is unknown but during the large number of measurements done on samples without nanoparticles, this behavior was never observed before. This makes it highly likely that, although it was not possible to qualitatively state what the influence of the

nanoparticles on the growth behavior is, it is possible that the presence of the nanoparticles increase and influence the crystal growth rate.

Conclusions The measurements are not conclusive but there are indications that the presence of the nanoparticles do increase the crystal growth rate. An important remark that has to be made here is that although the growth rates measured in each area are similar, the higher reflection of the nanoparticles means that less light is absorbed by the phase-change material. This means that the temperature increase due to the direct laser light is expected to be less. Based on this, the crystal growth rate is expected to be less in these areas. The fact that we do see similar growth rates makes it plausible that the nanoparticles do have an important influence.

Further research is required to analyze this problem in detail and to discern what the influence of the nanoparticles precisely is. The first issue that would have to be solved is the reduction of the reflection of the laser light. Also it is seen that this method of spreading the nanoparticles on the surface results in locally high concentrations and poor distribution of the nanoparticles. Other ways to improve the distribution have to be found. A possible way to achieve this is to incorporate the nanoparticles in the phase-change material during the deposition of the film. An other way would be to first deposit the nanoparticles and then deposit the phase-change film on top of the nanoparticles.

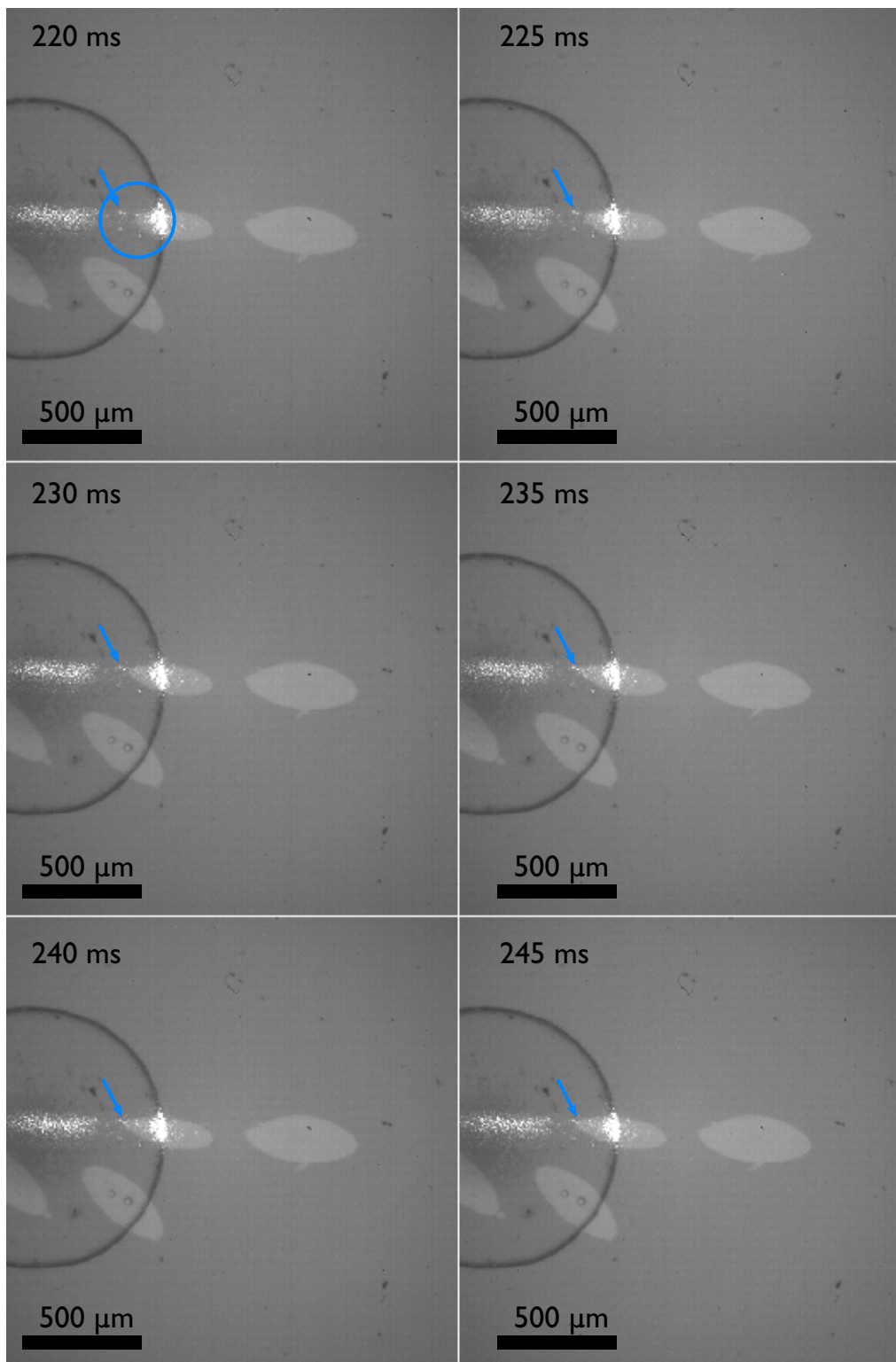


Figure 18: For one of the measurements an interesting phenomenon is observed. The time indicated is the time after which the laser pulse was switched on. The area of interest is marked by the circle. It is seen that in the course of 25 ms the crystal suddenly grows towards the point indicated by the arrows. This behavior has never been seen in a previous measurement. Also it is seen that the laser beam is reflected very strongly by the nanoparticles and the stabilizer molecules.

6 Conclusions

The crystal growth rate in thin films of $\text{Ge}_x\text{Sb}_{1-x}$, with compositions $x = 6, 7, 8, 9, 10$, has been successfully measured at temperatures beyond what was possible before using a hot-stage. By focusing a laser beam we were able to narrow a laser spot from $1000 \mu\text{m} \times 440 \mu\text{m}$ to $250 \mu\text{m} \times 110 \mu\text{m}$. Therefore it was possible to obtain higher temperatures at the locally irradiated area and thus achieve higher crystal growth rates. Combining the new measurements with the measurements obtained by Gert Eising, i.e. isothermal and large laser spot measurements, we have observed deviation from the Arrhenius behavior which was observed at lower temperatures. Because it was not possible to measure the local temperature during the measurements directly an indirect approach was used. By assuming Arrhenius behavior within the measured temperature range for the lowest germanium containing composition, $\text{Ge}_6\text{Sb}_{94}$, we were able to estimate the added laser heat by the laser. Using this estimation we determined the local temperature during the measurements for the other compositions, $\text{Ge}_7\text{Sb}_{93}$, $\text{Ge}_8\text{Sb}_{92}$, $\text{Ge}_9\text{Sb}_{91}$ and $\text{Ge}_{10}\text{Sb}_{90}$.

To extrapolate the crystal growth rate to temperatures beyond the measurement range we transformed to viscosity and modeled according to the popular VFT model and a more recently suggested model, the Mauro model. Here we were able to obtain the fragility, $m = 46-68$ (Mauro) and $m = 60-109$ (VFT), and the glass temperatures, $T_g = 324-430$ (Mauro) and $T_g = 331-443$ (VFT) for all compositions. During the fitting the viscosity at infinite temperature was fixed, $\eta_\infty = -3$, as argued by Mauro et al. [38]. We observe that with the VFT model consequently higher values for the fitting parameters are obtained as is consistent with the findings of Mauro et al. Reversing the viscosity back to the crystal growth rate we obtain an estimate for the whole temperature range up to the melting temperature. Corresponding to the higher obtained fitting parameters using the VFT model, the estimated maximum crystal growth rate is consequently lower for each composition, $\sim 2 \text{ m s}^{-1}$ (VFT) versus $\sim 10 \text{ m s}^{-1}$ (Mauro). Albeit there are differences in results, the difference between the models in maximum growth rate remains small.

Although the results are reasonable, the obtained values for the maximum growth rate are not as expected. Earlier work done by Adelerhof [45] showed a maximum growth rate of 58 m s^{-1} for $\text{Ge}_{10}\text{Sb}_{90}$. To explain the observed difference we note that the measurements done in this research were done on as-deposited films whereas the results in ref [45] were obtained from measuring melt-quenched films. Earlier work done by Van Pieterse [48] and Oosthoek [49] show that the same crystal growth rate in melt-quenched films occur at lower temperatures compared with as-deposited films.

While the presented results are reasonable in their own right, the practical value is limited. In real life applications as a DVD rewritable, the state of the films will always be melt-quenched. The results presented here could thus best be seen as a good lower bound of the possibilities presented by this new type of material. Comparing $\text{Ge}_x\text{Sb}_{1-x}$ compositions with the popular $\text{Ge}_2\text{Sb}_2\text{Te}_5$ it is seen that the studied compositions show both drawback and advantages. GeSb compositions show increased phase separation and therefore reduced cell endurance. As advantage however the compositions show more potential when considering crystal growth. More research is needed to counter the drawbacks and identify the best composition for practical purposes.

A side track was taken where the influence of gold nanoparticles, which were applied to the surface of a $\text{Ge}_8\text{Sb}_{92}$ sample, was analyzed. Due to high reflectivity of the nanoparticles, irradiated at their resonance frequency pertaining to localized surface plasmon resonance, it was not possible to accurately measure the crystal growth rate. Therefore it was not possible to conclude whether the presence of the nanoparticles contributed to an increased crystal growth rate. However some deviating behavior was observed during one of the measurements which make it plausible that the nanoparticles in fact do influence the crystal growth rate. Further research has to be conducted to determine the precise effect of the nanoparticles.

7 Recommendations

A start has been made with uncovering the phase-change properties of the $\text{Ge}_x\text{Sb}_{1-x}$ compositions. Much more research can be done to obtain a complete understanding of the behavior of the material. While this research has mainly focused on as-deposited thin films, it would be very interesting to study the behavior of melt-quenched thin films and in that extend the cyclability of the material. As stated before the melt-quenched films are expected to show the same crystal growth speed as the as-deposited films for lower temperature. This also implies that the maximum attainable growth speed will be higher than with as-deposited films. This will also most likely mean however that the maximum operating temperature will drop as the material will also more easily crystallize when at lower temperatures. One way to attain melt-quenched films is with a setup that can switch the material to the amorphous state again. Amorphizing a thin film is done by heating the film above the melting temperature and quickly cooling the thin film again. This effectively 'freezes' the film in an amorphous state. The film is then melt-quenched.

An extend on this is to measure the cyclability of the material. When implemented in real applications, especially PRAM applications, the thin films will have to sustain more than 100000 read and write cycles. Especially because the GeSb alloys are more prone to phase separation, it is very interesting to find out the limits of the alloys. With a setup that can crystallize and amorphize the material endurance tests can be performed.

A main issue during this research was measuring the local temperature during the measurement. As the sample is only locally heated at the location where the laser irradiates the film, the temperature has to be measured very accurate, exactly in the area which is heated by the laser. This is very difficult to accomplish. One way to circumvent this issue and measure the crystal growth rate at higher temperatures is reported by Salinga et al [39]. The method consists of writing an amorphous mark on a completely crystalline sample. To write a circular amorphous mark, the sample is heated to high temperatures and cooled within tens of nanoseconds to the stage temperature. The mark then recrystallizes from the edges towards the center of the mark. The crystal growth rate can then be measured up to much higher temperatures. The limit of this approach is the time necessary to recrystallize the sample which has to be higher than the tens of nanoseconds it takes to cool the sample to the stage temperature. Also the time necessary to do an accurate measurement needs to be taken into account. All in all this approach allows for accurate measurements up to much higher temperatures than was previously possible.

An other approach would be to measure the temperature directly using a temperature measuring device such as a pyrometer. The main issue with this approach would be to align the pyrometer accurately at the area which is irradiated with the laser. Whether this is viable approach has not been tested.

8 References

- [1] S. R. Ovshinsky, "Reversible electrical switching phenomena in disordered structures", *Phys. Rev. Lett.*, vol. 21, pp. 1450–1453, Nov 1968.
- [2] M. Chen, K. A. Rubin and R. W. Barton, "Compound materials for reversible, phase-change optical data storage", *Applied Physics Letters*, vol. 49, no. 9, pp. 502–504, 1986.
- [3] N. Yamada, E. Ohno, N. Akahira, K. Nishiuchi, K. Nagata and M. Takao, "High speed overwriteable phase change optical disk material", *Japanese Journal of Applied Physics*, vol. 26S4, no. Supplement 26-4, pp. 61–66, 1987.
- [4] N. Yamada, M. Takao and M. Takenaga, "Te-Ge-Sn-Au phase change recording film for optical disk", *Proc. SPIE*, vol. 0695, pp. 79–85, 1987.
- [5] E. Ohno, N. Yamada, T. Kurumizawa, K. Kimura and M. Takao, "TeGeSnAu alloys for phase change type optical disk memories", *Japanese Journal of Applied Physics*, vol. 28, no. Part 1, No. 7, pp. 1235–1240, 1989.
- [6] N. Yamada, E. Ohno, K. Nishiuchi, N. Akahira and M. Takao, "Rapid-phase transitions of GeTe-Sb₂Te₃ pseudobinary amorphous thin films for an optical disk memory", *Journal of Applied Physics*, vol. 69, no. 5, pp. 2849–2856, 1991.
- [7] H. Iwasaki, Y. Ide, M. Harigaya, Y. Kageyama and I. Fujimura, "Completely erasable phase change optical disk", *Japanese Journal of Applied Physics*, vol. 31, no. Part 1, No. 2B, pp. 461–465, 1992.
- [8] M. Horie, N. Nobukuni, K. Kiyono and T. Ohno, "High-speed rewritable DVD up to 20 m/s with nucleation-free eutectic phase-change material of Ge(Sb₇₀Te₃₀)+Sb", *Proc. SPIE*, vol. 4090, pp. 135–143, 2000.
- [9] T. Kato, H. Hirata, T. Komaki, H. Inoue, H. Shingai, N. Hayashida and H. Utsunomiya, "The phase change optical disc with the data recording rate of 140Mbps", *Japanese Journal of Applied Physics*, vol. 41, no. Part 1, No. 3B, pp. 1664–1667, 2002.
- [10] H. Iwasaki, M. Harigaya, O. Nonoyama, Y. Kageyama, M. Takahashi, K. Yamada, H. Deguchi and Y. Ide, "Completely erasable phase change optical disc ii: Application of Ag-In-Sb-Te mixed-phase system for rewritable compact disc compatible with CD-velocity and double CD-velocity", *Japanese Journal of Applied Physics*, vol. 32, no. Part 1, No. 11B, pp. 5241–5247, 1993.
- [11] C. N. Afonso, J. Solis, F. Catalina and C. Kalpouzou, "Ultrafast reversible phase change in GeSb films for erasable optical storage", *Applied Physics Letters*, vol. 60, no. 25, pp. 3123–3125, 1992.
- [12] M. Wuttig, "Phase-change materials: Towards a universal memory?", *Nature*, vol. 5, no. 4, pp. 265–266, 2005.
- [13] Y. Chen, C. Rettner, S. Raoux, G. Burr, S.-H. Chen, R. Shelby, M. Salinga, W. Risk, T. Happ, G. McClelland, M. Breitwisch, A. Schrott, J. Philipp, M.-H. Lee, R. Cheek, T. Nirschl, M. Lamorey, C. Chen, E. Joseph, S. Zaidi, B. Yee, H. L. Lung, R. Bergmann and C. Lam, "Ultra-thin phase-change bridge memory device using GeSb", in *Electron Devices Meeting, 2006. IEDM '06. International*, pp. 1–4, Dec 2006.
- [14] W. Y. Cho, B.-H. Cho, B.-G. Choi, H.-R. Oh, S. Kang, K.-S. Kim, K.-H. Kim, D.-E. Kim, C.-K. Kwak, H.-G. Byun, Y. Hwang, S. Ahn, G.-H. Koh, G. Jeong, H. Jeong and K. Kim, "A 0.18 μ m 3.0V 64Mb nonvolatile phase-transition random access memory (PRAM)", *Solid-State Circuits, IEEE Journal of*, vol. 40, pp. 293–300, Jan 2005.

- [15] A. Pirovano, A. Lacaíta, A. Benvenuti, F. Pellizzer and R. Bez, "Electronic switching in phase-change memories", *Electron Devices, IEEE Transactions on*, vol. 51, pp. 452–459, March 2004.
- [16] F. Merget, D. Kim, P. Bolivar and H. Kurz, "Lateral phase change random access memory cell design for low power operation", *Microsystem Technologies*, vol. 13, no. 2, pp. 169–172, 2007.
- [17] D.-H. Kim, F. Merget, M. Först and H. Kurz, "Three-dimensional simulation model of switching dynamics in phase change random access memory cells", *Journal of Applied Physics*, vol. 101, no. 6, pp. –, 2007.
- [18] M. Wuttig and M. Salinga, "Phase-change materials: Fast transformers", *Nat Mater*, vol. 11, no. 4, pp. 270–271, 2012.
- [19] S. Arrhenius, "Über die dissociationswärme und den einfluß der temperatur auf den dissociationsgrad der elektrolyte", *Z. Physik. Chem.*, vol. 4, pp. 96–116, 1889.
- [20] S. Arrhenius, "Über die reaktionsgeschwindigkeit bei der inversion von rohrzucker durch säuren", *Z. Physik. Chem.*, vol. 4, pp. 226–248, 1889.
- [21] M. Volmer and A. Weber, "Nucleation of supersaturated structures", *Z. Physik. Chem.*, vol. 119, pp. 277–301, 1926.
- [22] R. Becker and W. Döring, "Kinetische behandlung der keimbildung in übersättigten dampfen", *Annalen der Physik (Leipzig)*, vol. 24, pp. 719–752, 1935.
- [23] A. Kolmogoroff, "A statistical theory for the recrystallization of metals", *Izv. Akad. Nauk SSSR Ser. Mat.*, vol. 1, pp. 355–359 (in Russian), 1937.
- [24] A. Shiryayev, *Selected works of A.N. Kolmogorov*, vol. II. Dordrecht: Kluwer Academic, 1992.
- [25] W. Johnson and M. R.F., "Reaction kinetics in processes of nucleation and growth", *Trans. AIME*, vol. 135, pp. 416–459, 1939.
- [26] M. Avrami, "Kinetics of phase change. I General theory", *The Journal of Chemical Physics*, vol. 7, no. 12, pp. 1103–1112, 1939.
- [27] M. Avrami, "Kinetics of phase change. II Transformation-time relations for random distribution of nuclei", *The Journal of Chemical Physics*, vol. 8, no. 2, pp. 212–224, 1940.
- [28] M. Avrami, "Granulation, phase change, and microstructure kinetics of phase change. III", *The Journal of Chemical Physics*, vol. 9, no. 2, pp. 177–184, 1941.
- [29] J. Christian, *The Theory of Transformations in Metals and Alloys*, vol. I. Oxford: Pergamon, 1975.
- [30] M. Von Heimendahl and G. Maussner, "The metastable crystallization phases in the amorphous alloy Metglas 2826A", *Journal of Materials Science*, vol. 14, no. 5, pp. 1238–1244, 1979.
- [31] R. Tiwari, S. Ranganathan and M. Von Heimendahl, "TEM of the kinetics of crystallization of Metglas 2826", *Zeitschrift für Metallkunde*, vol. 72, no. 8, pp. 563–568, 1981.
- [32] S. Ranganathan and M. Von Heimendahl, "The three activation energies with isothermal transformations: applications to metallic glasses", *Journal of Materials Science*, vol. 16, no. 9, pp. 2401–2404, 1981.
- [33] M. von Heimendahl and G. Kuglstätter, "The activation energies of crystallization in the amorphous alloy Metglas 2826A", *Journal of Materials Science*, vol. 16, no. 9, pp. 2405–2410, 1981.
- [34] P. Boswell, "The effect of thermal history on the crystallization kinetics of a liquid-quenched metallic glass", *Journal of Materials Science*, vol. 15, no. 8, pp. 1939–1946, 1980.

- [35] G. Ruitenberg, A. K. Petford-Long and R. C. Doole, "Determination of the isothermal nucleation and growth parameters for the crystallization of thin Ge₂Sb₂Te₅ films", *Journal of Applied Physics*, vol. 92, no. 6, pp. 3116–3123, 2002.
- [36] D. Porter and K. Easterling, *Phase transformations in metals and alloys*. New York: Van Nostrand Reinhold Company Ltd., 1st ed., 1981.
- [37] G. W. Scherer, "Editorial comments on a paper by Gordon S. Fulcher", *Journal of the American Ceramic Society*, vol. 75, no. 5, pp. 1060–1062, 1992.
- [38] J. C. Mauro, Y. Yue, A. J. Ellison, P. K. Gupta and D. C. Allan, "Viscosity of glass-forming liquids", *Proceedings of the National Academy of Sciences*, vol. 106, no. 47, pp. 19780–19784, 2009.
- [39] M. Salinga, E. Carria, A. Kaldenbach, M. Bornhöfft, J. Benke, J. Mayer and M. Wuttig, "Measurement of crystal growth velocity in a melt-quenched phase-change material", *Nature Communication*, vol. 4, 8 2013.
- [40] D. Turnbull and J. C. Fisher, "Rate of nucleation in condensed systems", *The Journal of Chemical Physics*, vol. 17, no. 1, pp. 71–73, 1949.
- [41] C. V. Thompson and F. Spaepen, "On the approximation of the free energy change on crystallization", *Acta Metallurgica*, vol. 27, no. 12, pp. 1855 – 1859, 1979.
- [42] G. Eising, *Crystallization phenomena in germanium antimony phase-change films*. PhD thesis, University of Groningen, 2013.
- [43] D. Dimitrov, C. Babeva, S.-T. Cheng, W.-C. Hsu, H. M.-H. and S.-Y. Tsai, "High-speed reversible phase-change optical recording in GeSb-based alloys", *European Phase Change Ovonic Science Symposium*, 2004.
- [44] J. L. Oosthoek, B. J. Kooi, J. T. De Hosson, R. A. Wolters, D. J. Gravesteijn and K. Attenborough, "Growth rate determination through automated TEM image analysis: Crystallization studies of doped SbTe phase-change thin films", *Microscopy and Microanalysis*, vol. 16, pp. 291–299, 6 2010.
- [45] D. J. Adelerhof, "Media development for DVD+RW phase change recording", *European Phase Change Ovonic Science Symposium*, 2004.
- [46] J. Kalb, *Crystallization kinetics in antimony and tellurium alloys used for phase change recording*. PhD thesis, Technischen Hochschule Aachen, 2006.
- [47] R. Olesinski and G. Abbaschian, "The ge–sb (germanium-antimony) system", *Bulletin of Alloy Phase Diagrams*, vol. 7, no. 3, pp. 219–222, 1986.
- [48] L. van Pieterse, M. H. R. Lankhorst, M. van Schijndel, A. E. T. Kuiper and J. H. J. Roosen, "Phase-change recording materials with a growth-dominated crystallization mechanism: A materials overview", *Journal of Applied Physics*, vol. 97, no. 8, 2005.
- [49] J. Oosthoek, B. Kooi, J. De Hosson, D. Gravesteijn, K. Attenborough, W. Rob and V. Marcel, "Crystallization studies of doped SbTe phase-change thin films and PRAMline cells: Growth rate determination by automated TEM image analysis", *European Phase Change Ovonic Science Symposium*, 2009.
- [50] O. Neumann, A. S. Urban, J. Day, S. Lal, P. Nordlander and N. J. Halas, "Solar vapor generation enabled by nanoparticles", *ACS Nano*, vol. 7, no. 1, pp. 42–49, 2013. PMID: 23157159.
- [51] Y. Gao, Z. Yuan and S. Gao, "Semiclassical approach to plasmon–electron coupling and Landau damping of surface plasmons", *The Journal of Chemical Physics*, vol. 134, no. 13, 2011.

- [52] E. Lukianova-Hleb, Y. Hu, L. Latterini, L. Tarpani, S. Lee, R. A. Drezek, J. H. Hafner and D. O. Lapotko, "Plasmonic nanobubbles as transient vapor nanobubbles generated around plasmonic nanoparticles", *ACS Nano*, vol. 4, no. 4, pp. 2109–2123, 2010. PMID: 20307085.
- [53] G. Baffou, R. Quidant and F. J. García de Abajo, "Nanoscale control of optical heating in complex plasmonic systems", *ACS Nano*, vol. 4, no. 2, pp. 709–716, 2010. PMID: 20055439.
- [54] Z. Fang, Y.-R. Zhen, O. Neumann, A. Polman, F. J. García de Abajo, P. Nordlander and N. J. Halas, "Evolution of light-induced vapor generation at a liquid-immersed metallic nanoparticle", *Nano Letters*, vol. 13, no. 4, pp. 1736–1742, 2013. PMID: 23517407.
- [55] A. Polman, "Solar steam nanobubbles", *ACS Nano*, vol. 7, no. 1, pp. 15–18, 2013. PMID: 23282196.